Nano Research

ISSN 1998-0124 CN 11-5974/O4
https://doi.org/10.26599/NR.2026.94908426

Research Article

Fe^{2+}-crosslinked MXene fibers for multifunctional electronic textile

Wenkun Fei[1,2,§], Xuejiao Wang[2,§], Chaoyang Miao[2,§], Jiahao Chen[2], Shujuan Liu[1], Bingxiang Li[2](✉), Jianmin Li[1,2](✉), Qiang Zhao[1,2](✉)

[1] State Key Laboratory of Flexible Electronics (LoFE) & Institute of Advanced Materials (IAM), Nanjing University of Posts & Telecommunications, Nanjing 210023, China

[2] College of Electronic and Optical Engineering & College of Flexible Electronics (Future Technology), Nanjing University of Posts & Telecommunications, Nanjing 210023, China

[§] Wenkun Fei, Xuejiao Wang, and Chaoyang Miao contributed equally to this work.

Nano Res., **Just Accepted Manuscript** • https://doi.org/10.26599/NR.2026.94908426

https://www.sciopen.com/journal/1998-0124 on Jan. 9, 2026

Just Accepted

TABLE OF CONTENTS (TOC)

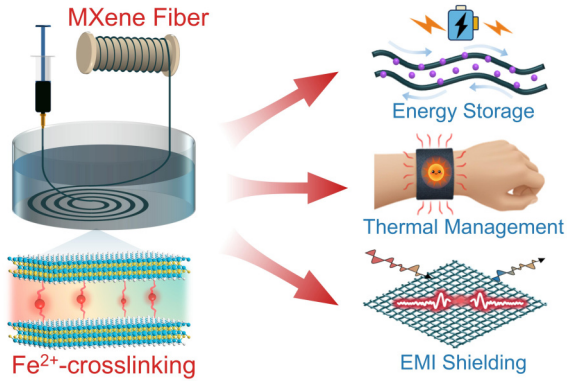

Fe^{2+}-crosslinked $Ti_3C_2T_x$ fibers integrate high strength and conductivity, enabling versatile wearable electronics

Nano Research

Open Access

Research Article

Fe^{2+}-crosslinked MXene fibers for multifunctional electronic textile

Wenkun Fei [1,2,§], Xuejiao Wang [2,§], Chaoyang Miao [2,§], Jiahao Chen [2], Shujuan Liu [1], Bingxiang Li [2] ✉, Jianmin Li [1,2] ✉, and Qiang Zhao [1,2] ✉

[1] *State Key Laboratory of Flexible Electronics (LoFE) & Institute of Advanced Materials (IAM), Nanjing University of Posts & Telecommunications, Nanjing 210023, China*

[2] *College of Electronic and Optical Engineering & College of Flexible Electronics (Future Technology), Nanjing University of Posts & Telecommunications, Nanjing 210023, China*

[§] *Wenkun Fei, Xuejiao Wang, and Chaoyang Miao contributed equally to this work.*

Received: 3 December 2025 **Revised:** 31 December 2025; **Accepted:** 9 January 2026

✉ Address correspondence to Bingxiang Li, bxli@njupt.edu.cn; Jianmin Li, lijm@njupt.edu.cn; Qiang Zhao, iamqzhao@njupt.edu.cn

Cite this article: *Nano Research*, **2026**, *19*, 94908426. https://doi.org/10.26599/NR.2026.94908426

ABSTRACT: The increasing demand for multifunctional wearable electronics and intelligent electronic textile systems necessitates advanced functional fibers that integrate mechanical durability, superior conductivity, and adaptive functionalities. Here, a Fe^{2+}-crosslinking strategy is employed to engineer structural-functional synergy in $Ti_3C_2T_x$ MXene fibers, through the coordination bridging effect between Fe^{2+} ions and $Ti_3C_2T_x$ surface functional groups. This design enhances interlayer interfacial coupling within the nanosheet framework, yielding highly aligned $Ti_3C_2T_x$ fibers with outstanding mechanical strength (143.7 MPa) and electrical conductivity (2607 S cm^{-1}), simultaneously. As a result, the fibers exhibit excellent Joule heating effect for wearable thermal management, reaching 122°C within 2 min at 2 V. For energy storage, the as-prepared fibers show remarkable pseudocapacitive charge storage capacity of 1239 F cm^{-3}, enabling fiber-shaped supercapacitors with a high energy density of 14.12 mWh cm^{-3} and peak power density of 6000.41 mW cm^{-3}, surpassing most previously reported MXene-based fiber devices. When woven into common textiles with programmable mesh architectures, the fabrics provide adjustable electromagnetic interference (EMI) shielding, with effectiveness up to 23.1 dB in a 1×1 cm^2 grid configuration. This multifunctional $Ti_3C_2T_x$ fiber offers a versatile platform for integrated thermal management, self-powered microsystems, and electromagnetic protection textiles, demonstrating significant potential for next-generation wearable electronics.

KEYWORDS: wearable electronics, electronic textile, multifunctional fibers, MXene, Fe^{2+}-crosslinking

1 Introduction

The rapid evolution of wearable electronics has catalyzed transformative advancements in human-machine interfaces, portable energy storage, and personalized healthcare, fundamentally redefining human-technology interaction frameworks [1-5]. Despite these advances, critical limitations persist in terms of wearing comfort, sustainable energy supply, and environmental adaptability [6-8]. Textile-based wearable electronic systems, often termed electronic textiles (e-textiles), represent promising solutions to these interdisciplinary challenges, leveraging their inherent breathability, skin-conformal characteristics, and seamless integration with garment architectures [9-11]. Consequently, the development of advanced functional fibers—serving as the core functional primitives for e-textiles—that synergize electronic functionality with textile-grade processability, has become a central focus in wearable electronics research [12-14].

Various materials have been explored for fabricating functional fibers, including metallic nanowires (e.g., silver nanowires (AgNWs)), conductive polymers (e.g., poly(3,4-ethylenedioxyhiophene)-poly(styrenesulfonate) (PEDOT: PSS)), and carbon allotropes (e.g., carbon nanotubes, graphene) [15,16]. However, previously reported functional fibers usually encounter inherent trade-offs among properties of electrical conductivity, mechanical robustness, and long-term environmental stability [17,18]. These limitations underscore the urgent need for novel material platforms.

Two-dimensional transition metal carbides/nitrides (MXenes), celebrated for their metallic conductivity and fertile surface chemistry, have recently emerged as highly promising candidates for next-generation functional fibers [19-21]. Notably, their hydrophilic surface allows them to form high-concentration dispersions to construct an aligned nematic liquid crystalline (LC) phase, which is critical for the continuous fabrication of MXene fibers by the wet-spinning technique. For instance, Gogotsi and co-workers reported neat $Ti_3C_2T_x$ MXene fibers via wet-spinning of additive-free LC inks, demonstrating high conductivity and energy storage ability [22]. However, the inherent weak van der Waals interlayer interactions among MXene sheets limit their mechanical strength and toughness, posing challenges for textile processing that involves repeated bending, stretching, and weaving.

Conventional reinforcement strategies through polymer blending or coaxial structuring often compromise electrical performance, re-entering the classic conductivity-strength

dilemma [23,24]. Overcoming this challenge necessitates sophisticated interfacial engineering to precisely tune interlayer interactions at the molecular or atomic level. Specifically, bridging adjacent nanosheets via specific molecules or ions has proven effective in enhancing mechanical robustness without significantly impairing electron transport pathways [25-27]. This suggests the possibility of fabricating MXene fibers with both high conductivity and robust mechanical properties by introducing ionic bridges among MXene nanosheets.

In this work, we demonstrate a Fe^{2+}-assisted dynamic assembly strategy to synergistically enhance the electronic conductivity and mechanical strength of $Ti_3C_2T_x$ MXene fibers. During the wet-spinning process, the divalent Fe^{2+} ions exhibit strong interaction with the surface groups of $Ti_3C_2T_x$, act as interfacial mediators to tightly bridge $Ti_3C_2T_x$ sheets. As a result, the fabricated fibers show a compact and aligned structure that constructs highly ordered electron transport pathways, inducing excellent conductivity of 2607 S cm^{-1}, as well as high mechanical strength of 143.7 MPa. In addition, the reductive Fe^{2+} ions can potentially protect the $Ti_3C_2T_x$ sheets from oxidation and degradation, enhancing the long-term performance and storage stability of the fibers. Notably, the as-prepared $Ti_3C_2T_x$ fibers show promising performance for applications in wearable energy storage, thermal management, and electromagnetic protection, which can also be readily woven into functional e-textiles. By engineering the nano-ionic interfaces within the fibers, this work presents a viable strategy for creating high-performance multifunctional fibers that can serve as foundational building blocks for the next generation of intelligent e-textiles and integrated wearable systems.

2 Results and discussion

2.1 Concept of the Fe^{2+}-assisted wet-spinning process.

As one of the most widely used methods for fabricating industrial fibers, wet spinning offers a scalable and efficient approach for assembling 2D $Ti_3C_2T_x$ nanosheets into continuous functional fibers [19,28]. During this process, a high-concentration $Ti_3C_2T_x$ dispersion is injected into $FeCl_2$ coagulation bath to form fibers under the drive of solvent exchange between the dispersion and coagulation bath (see Fig. 1(a)). Notably, the Fe^{2+} ions, which have been reported to show strong crosslinking interaction with $Ti_3C_2T_x$ flakes, are introduced into the coagulation bath ($FeCl_2$ solution) to implement a hierarchical structural regulation strategy that governs the overall performance of the fibers [29,30].

Briefly, the spinning process involves three sequential stages: (1) entropy-driven formation of a directionally aligned nematic LC phase within high-concentration $Ti_3C_2T_x$ dispersions, constructing an ordered precursor system; (2) shear stress-induced axial alignment of nanosheets during extrusion through the capillary tunnel, to further enhance the orderliness; and critically; (3) Fe^{2+}-mediated interlayer

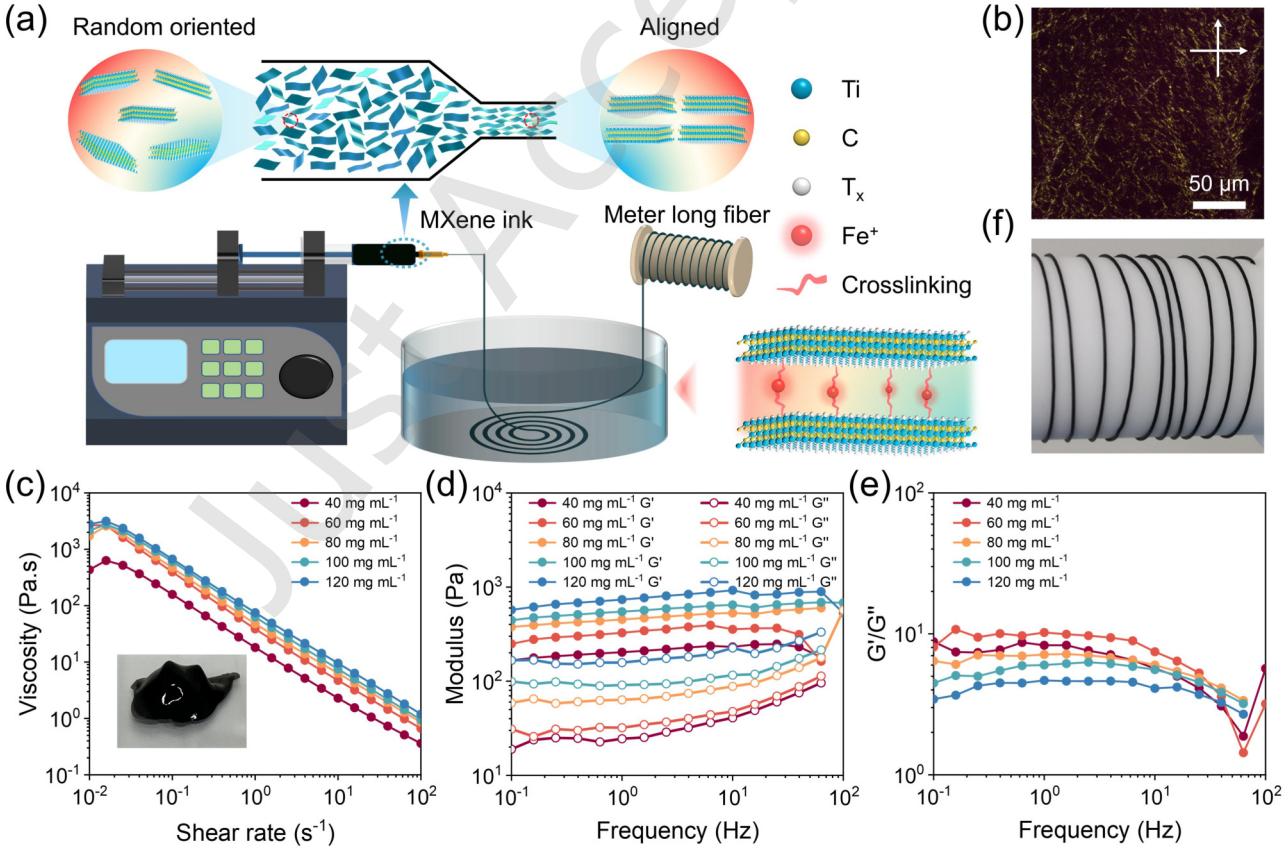

Figure 1. Preparation of Fe^{2+}-crosslinked $Ti_3C_2T_x$ MXene fibers. (a) Schematic illustration of the wet spinning process. (b) POM image of 80 mg mL^{-1} $Ti_3C_2T_x$ dispersion. (c) Viscosity versus shear rate, (d) elastic modulus (G') and viscous modulus (G'') versus frequency, and (e) G'/G'' ratio versus frequency for $Ti_3C_2T_x$ spinning solutions at different concentrations, with an inset digital photograph of the 80 mg mL^{-1} $Ti_3C_2T_x$ solution. (f) Digital photograph of a continuous meter-long $Ti_3C_2T_x$ fiber collected by spooling.

crosslinking during the dynamic solvent exchange in the $FeCl_2$ congulation bath, yielding highly oriented lamellar architectures. The strong interaction between Fe^{2+} ions and $Ti_3C_2T_x$ nanosheets, facilitated by coordination bonding with surface functional

groups (=O, -OH), is crucial for initiating rapid coagulation, which simultaneously stabilizes and compacts the aligned structure during spinning [29,30]. By combining these three synergistic processes, the mechanical strength of the fiber could be significantly enhanced, while the electronic pathways are optimized for better conductivity.

The formation of stable, high-concentration dispersion is a critical precondition for fabricating high-quality $Ti_3C_2T_x$ fibers. The monolayer $Ti_3C_2T_x$ nanosheets with good dispersibility in water were synthesized via a modified minimal intensive layer delamination (MILD) method (detailed in the Method section) [31]. Scanning electron microscopy (SEM) images clearly revealed the morphological evolution from the pristine Ti_3AlC_2 MAX phase to the final $Ti_3C_2T_x$ MXene. The pristine MAX phase exhibited a dense, layered bulk structure (Fig. S1a). After etching and exfoliation, $Ti_3C_2T_x$ MXene nanosheets with a typical 2D layered structure with large lateral dimensions were successfully obtained (Fig. S1b). In addition, the X-ray diffraction (XRD) pattern further verified the successful etching and exfoliation, as evidenced by the complete disappearance of the pristine MAX phase (104) peak and the left shift of the (002) peak (Fig. S1c).

According to Onsager's *excluded volume theory*, dispersions of high-aspect-ratio nanosheets, like $Ti_3C_2T_x$, undergo entropy-driven spontaneous alignment into nematic LC phase when their concentration exceeds a critical threshold [32-35]. Polarized optical microscopy (POM) was conducted on $Ti_3C_2T_x$ dispersions with concentrations ranging from 40 to 120 mg mL^{-1}. As shown in Fig. 1(b) and S2 in the Electronic Supplementary Material (ESM), distinct birefringence patterns, characteristic of LC phases, were observed across this range, while more dilute dispersions failed to form continuous LC domains. The birefringence should arise from the long-range orientational order of the $Ti_3C_2T_x$ nanosheets. Notably, the 80 mg mL^{-1} dispersion exhibits maximum birefringence intensity, indicating an optimal balance: the concentration is high enough to drive entropy-led alignment, yet not so high as to cause excessive aggregation that would disrupt the nematic order. This enhanced nematic order is crucial as it facilitates better alignment of nanosheets during the spinning process, directly contributing to the structural integrity and performance of the final fibers [36].

Rheological analysis elucidates the shear-induced evolution of $Ti_3C_2T_x$ dispersions with various concentrations, which is equally critical for ensuring continuous and stable fiber formation. Shear rate-dependent viscosity profiles reveal pronounced shear-thinning behavior across all concentrations (Fig. 1(c)), which can be attributed to the shear-induced disentanglement and flow-aligned reorientation of $Ti_3C_2T_x$ nanosheets. All dispersions exhibit high zero-shear viscosity (e.g., 1725.57 Pa·s for the 80 mg mL^{-1} dispersion at 0.01 s^{-1}), conferring structural rigidity to maintain the aligned LC domain integrity during the extrusion stage of the wet-spinning process. Dynamic oscillatory tests further demonstrate frequency-dependent viscoelastic responses (Fig. 1(d) and (e)). The elastic modulus (G') consistently dominates over the viscous modulus (G'') across 0.1-100 Hz, with G'/G'' >1, signifying predominantly solid-like viscoelastic behavior. This elastic dominance ensures shape retention during extrusion, preventing jet breakup due to surface tension-induced capillary rupture [37,38]. In addition, the "shear alignment-elastic solidification" kinetics underpins the transition from disordered nanosheets to a highly aligned fiber matrix.

The meter-scale $Ti_3C_2T_x$ fibers were continuously fabricated under the drive of Fe^{2+}-mediated crosslinking effect, by extruding the dispersion into the $FeCl_2$ coagulation bath (see Fig. 1(f) and Movie S1). This process can be understood from a multiscale perspective. Upon injection into the bath, the fiber-shaped $Ti_3C_2T_x$ slurry undergoes dynamic solvent exchange, triggering multiscale ionic crosslinking. At the colloidal scale, Fe^{2+} ions electrostatically attract the negatively charged surface of $Ti_3C_2T_x$, reducing the Debye-Hückel-Landau-Verwey-Overbeek (DLVO) repulsion barrier and initiating rapid coagulation [39]. Concurrently, at the atomic level, more specific and robust coordination bonds form between Fe^{2+} ions and oxygen-containing groups (=O/−OH) on adjacent nanosheets [29]. This powerful short-range interaction acts as a "molecular rivet", tightly linking the nanosheets together to restrict their slippage and stabilize the axially aligned structure achieved during shear flow [40]. This engineered, compact, and highly ordered structure is expected to yield enhanced mechanical robustness and electronic conductivity. Notably, the mild reducing capacity of Fe^{2+} also facilitates preferential electron transfer with oxidative species, promising to form a protective barrier against the hydrolytic/oxidative degradation of $Ti_3C_2T_x$ flakes.

2.2 Characterizations of the $Ti_3C_2T_x$ fiber

To screen out the optimal spinning process parameters, we first examined the effect of spinning dope concentration (40-120 mg mL^{-1}) on the structure and properties of $Ti_3C_2T_x$ MXene fibers, using a fixed $FeCl_2$ concentration of 0.1 mol L^{-1} in the coagulation bath. As shown in Fig. S6 and S7, surface and cross-section SEM images reveal the wrinkled surface texture and aligned stacking of 2D nanosheets inside all fibers. The formation of this wrinkled surface texture is attributed to the differential crosslinking kinetics and radial heterogeneity. The diffusion-controlled solidification creates a rigid skin layer, which subsequently buckles under the compressive stress induced by the volume contraction of the inner core during drying. Notably, the fibers fabricated by low-concentration dopes (40-60 mg mL^{-1}) show relatively compact structure but irregular cross-sections, which should be resulted from their rapid gelation in the coagulation bath due to insufficient nanosheet density. Besides, excessive concentrations (100-120 mg mL^{-1}) cause overall structural looseness and random agglomeration, hindering the formation of a continuous network. The fiber prepared at 80 mg mL^{-1} exhibits the optimal balance of structural integrity and nanosheet alignment, yielding the highest tensile strength (Fig. S8a) and electrical conductivity (Fig. S8b). Specifically, the mechanical strength and conductivity increase from 74.6 MPa and 1469 S cm^{-1} at 40 mg mL^{-1} to peak values of 143.7 MPa and 2607 S cm^{-1} at 80 mg mL^{-1} respectively, followed by a decline at higher concentrations

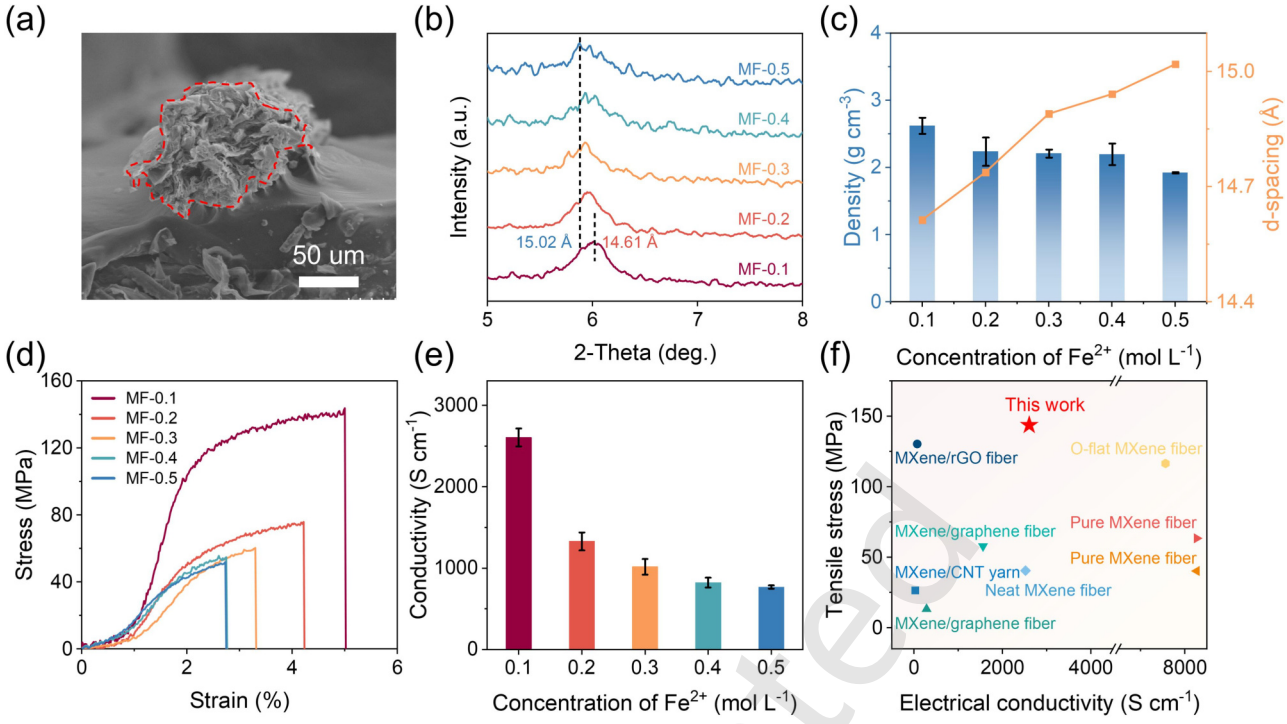

Figure 2 Microstructure and electrical/mechanical properties of $Ti_3C_2T_x$ fibers. (a) Cross-sectional SEM image of MF-0.1 fiber. (b) XRD patterns of MF-X fibers. (c) Effect of Fe^{2+} concentration on fiber density and d-spacing of $Ti_3C_2T_x$ flakes. (d) Stress-strain curves and (e) electrical conductivity of the MF-X fibers. (f) Comparison of electrical conductivity and tensile strength between MF-0.1 and previously reported MXene-based fibers [19,22,28,41-45].

due to the increased viscosity-induced structural defects. Based on the above results, 80 mg mL^{-1} was adopted as the optimal spinning concentration in subsequent experiments.

To further probe the influence of Fe^{2+}-crosslinking on the structure and properties of the fibers, a series of $Ti_3C_2T_x$ MXene fibers (denoted as MF-X, where X represents the concentration of Fe^{2+} ions) were fabricated by varying the $FeCl_2$ concentration in the coagulation bath from 0.1 to 0.5 mol L^{-1}. As shown in Fig. 2(a), S3 and S4 in the ESM, all MF-X fibers also exhibit wrinkled surface texture and ordered stacking of 2D nanosheets can be observed. However, both the roughness and porosity increase with the increased $FeCl_2$ concentration. Thus, the diameter of fibers increases from ~62 μm (MF-0.1) to ~111 μm (MF-0.5) (see Fig. S5 in the ESM). Notably, despite this concentration-dependent diameter increase, the final diameter of all fibers is significantly smaller than the spinneret orifice (500 μm). This reduction arises from the combined effects of the strong Fe^{2+}-crosslinking effect which pulls the nanosheets into a highly compact arrangement, the axial drawing force applied during collection which stretches the fiber, and the substantial volume shrinkage loss from solvent evaporation during drying. Interestingly, the increase in diameter is consistent with the microscopic structure (interlayer spacing) changes revealed by XRD results (see Fig. 2(b)). The (002) diffraction peak progressively shifts to lower angles, from 6.06° of MF-0.1 to 5.88° of MF-0.5, corresponding to an interlayer spacing expansion from 14.61 Å to 15.02 Å. As a direct consequence, the overall packing density of the fibers decreases from 2.6 g cm^{-3} to 1.9 g cm^{-3} (Fig. 2(c)).

This concentration-dependent structural evolution should be governed by the kinetics of the coagulation process. At the molecular level, Fe^{2+} ions diffuse into the precursor fiber and coordinate with surface functional groups on $Ti_3C_2T_x$ nanosheets to enhance the adhesion strength among MXene flakes and create a compact structure. The diffusion rate should be affected by the concentration of coagulation bath, which further influences the bonding speed and strength between Fe^{2+} and $Ti_3C_2T_x$ nanosheets, leading to diverse microstructures. At lower Fe^{2+} concentration, the osmotic pressure difference between the spinning dope and the bath is relatively small, leading to a slower rate of solvent exchange and ion diffusion. This slower process provides sufficient time for $Ti_3C_2T_x$ nanosheets to reorganize through coordination bonding and therefore self-assembly into a highly ordered and tightly packed configuration. In contrast, at high concentrations, the large osmotic pressure difference drives rapid solvent exchange and a surge of Fe^{2+} ions, which triggers an almost instantaneous solidification that kinetically traps the nanosheets in a less organized, loosely packed state.

The fiber's microstructure influences the arrangement of $Ti_3C_2T_x$ flakes, which therefore determines the mechanical and electrical properties to a great extent. The stress-strain curves reveal that the overall mechanical performance is highly dependent on the concentration of Fe^{2+} ions introduced during coagulation (Fig. 2(d) and Table S1 in the ESM). Specifically, the MF-0.1 fiber delivers the highest tensile strength of 143.7 MPa, Young's modulus of 10.4 GPa, and tensile toughness (capacity for energy absorption) of 4.57 MJ m^{-3}, reflecting the combination of high strength and ability to undergo moderate elongation. With the Fe^{2+} concentration increasing, the mechanical properties gradually decrease, as the tensile strength, Young's modulus, and tensile toughness of MF-0.5 decline to 51.9 MPa, 2.73 GPa and 0.73 MJ m^{-3}, respectively. These results are in agreement with the trend of fiber density, indicating that slow solvent exchange at low Fe^{2+} concentrations facilitates the formation of a well-aligned nanosheet framework to induce optimized performance. Within this compact configuration, Fe^{2+} crosslinks create

strong interlayer cohesion between the tightly stacked nanosheets. Such enhanced binding ensures effective stress transfer and uniform stress distribution across the nanosheet layers, minimizing stress concentration and suppressing interfacial slippage, which in turn reinforces the overall load-bearing capacity of the fiber [46-48].

Besides, the stress-strain curves all contain three stages: an initial quasi-linear region (elastic region), followed by a strain hardening phase where the slope increases, and finally a softening region that leads to fracture. In the initial elastic region, the Fe^{2+} coordination bonds contribute to maintaining structural integrity and enabling collective deformation. The subsequent non-linear strain-hardening region likely involves progressive slippage and rearrangement of $Ti_3C_2T_x$ nanosheets, accompanied by the breaking of coordination bonds under increasing strain [46,49]. Notably, this process occurs in a more orderly fashion for MF-0.1 because of the moderate crosslinking and dense stacking, allowing the structure to dissipate energy efficiently and sustain larger strains. As the fiber approaches its ultimate tensile limit, the curve flattens until fracture occurs, marking the exhaustion of load-bearing capacity. In contrast, the looser packing and weaker interlayer adhesion under higher Fe^{2+} concentrations facilitate interfacial slippage and stress localization. This leads to shorter elastic region, less pronounced strain-hardening effect, and more disordered nanosheet rearrangement, collectively contributing to the observed reduction in strength, stiffness, and toughness.

Also benefiting from its optimized orientation of $Ti_3C_2T_x$ flakes, the MF-0.1 fiber exhibits superior conductivity among the as-prepared fibers, reaching 2607 S cm^{-1} (Fig. 2(e)). The dense, highly aligned packing of the $Ti_3C_2T_x$ nanosheets creates continuous and ordered pathways for electron transport along the fiber axis, which minimizes tortuosity and reduces the resistance associated with inter-sheet electron hopping, thereby enhancing the conductivity [50]. The expanded interlayer spacing and looser packing induce relatively disordered structures under high Fe^{2+} concentration, which thus increase the barriers for carrier hopping and introduce more scattering sites to collectively hinder efficient charge transport. As a result, the electrical conductivity gradually decreases with the increased concentration, reaching 767 S cm^{-1} for MF-0.5. Thus, both the mechanical strength and electrical conductivity are synergistically enhanced via the crosslinking effect of Fe^{2+}, inducing superior performance among most reported neat or even composite MXene-based fibers (Fig. 2(f)).

2.3 Application for Energy Storage

Benefiting from its metallic conductivity and fertile surface chemistry, $Ti_3C_2T_x$ MXene has been widely used as one of the promising electrode materials for supercapacitors, whose 2D stacking structure also provides space for ion insertion [51]. Thus, $Ti_3C_2T_x$-based materials show significant pseudocapacitive performance to induce high capacitance and rate capability. In this work, besides the optimized conductivity and mechanical strength, the Fe^{2+} ion bridges may enlarge the interlayer spacing of $Ti_3C_2T_x$ flakes to facilitate the intercalation and further enhance the energy storage ability. In addition, the strong crosslinking force provided by Fe^{2+} ions would protect the fibers from structural

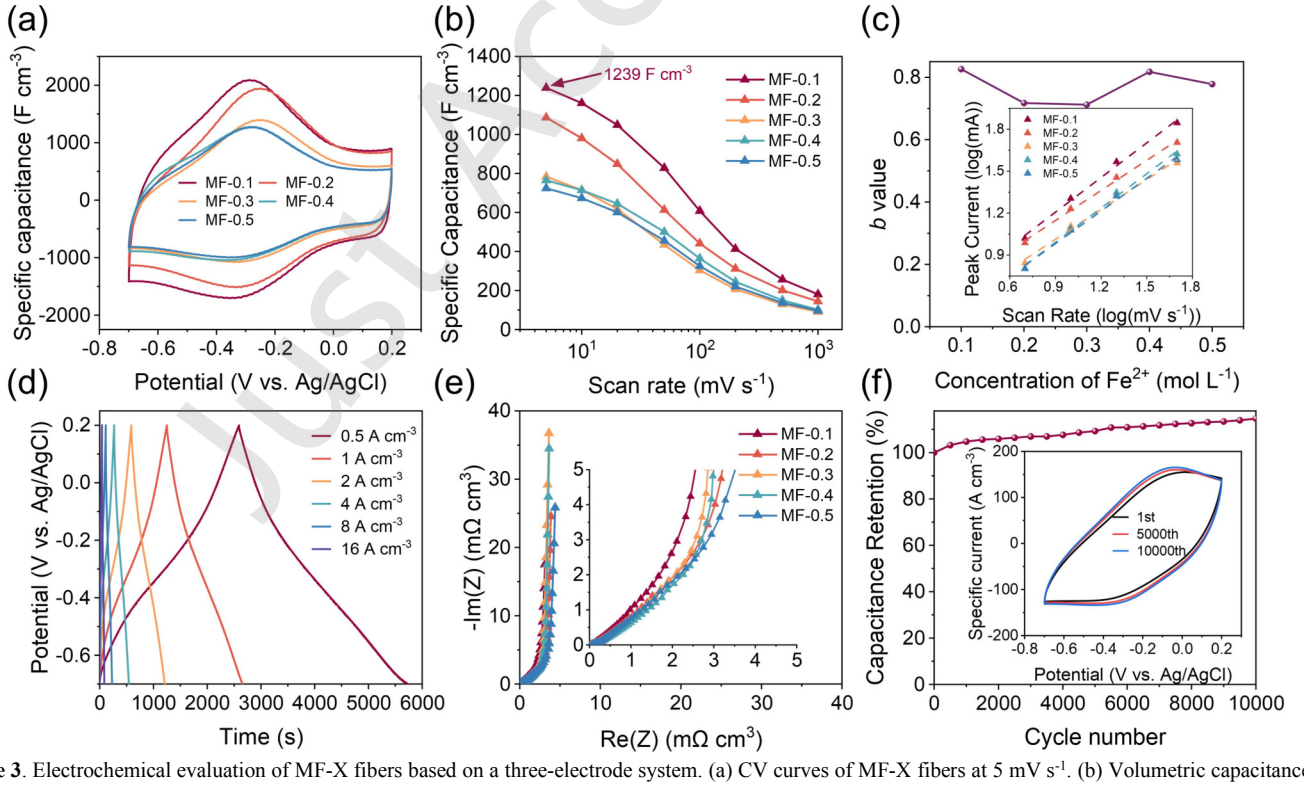

Figure 3. Electrochemical evaluation of MF-X fibers based on a three-electrode system. (a) CV curves of MF-X fibers at 5 mV s^{-1}. (b) Volumetric capacitances of MF-X fibers versus scan rates. (c) Power-law exponent b values of MF-X fibers (inset: log(peak current) vs. log(scan rate) plots). (d) GCD curves of MF-0.1 fibers at different current densities. (e) Nyquist plots for MF-X fibers, with the inset providing a magnified view of the high-frequency region. (f) Cyclic stability of MF-0.1 over 10,000 cycles, with the inset showing CV curves for the 1st, 5000th, and 10,000th cycles.

degradation during charge/discharge and deformation cycling, to provide good cycle and mechanical stability. Thus, the MF-X fibers were employed as capacitive electrodes and tested in 1 M H_2SO_4 electrolyte, to evaluate their electrochemical performance.

As shown in Fig. 3(a), all of the fibers exhibit cyclic voltammetry (CV) curves at a scan rate of 5 mV s^{-1} with obvious redox peaks (pseudocapacitive behavior), corresponding to the adsorption/desorption of protons and redox reactions on the $Ti_3C_2T_x$ surface [52]. The MF-0.1 fiber demonstrates the largest CV area and distinct redox peaks, reflecting its superior charge storage capacity and favorable reaction kinetics, which gradually decrease with higher Fe^{2+} concentration. In addition to the high conductivity, the interlayer spacing of $Ti_3C_2T_x$ flakes may play a critical role, since appropriately sized micropores have been proven to facilitate the desolvation process of hydrated ions during the intercalation, thereby improving capacity [53]. As a result, the relatively narrow interlayer spacing of the compact MF-0.1 fiber could enhance its energy storage ability by optimizing the intercalation process.

To evaluate their rate capability, the MF-X fibers were tested across various scan rates of 5-1000 mV s^{-1} (see Fig. S9 in the ESM). The CV curves maintain a quasi-rectangular shape even at 1000 mV s-1, highlighting efficient H^+ transport and rapid redox kinetics [40]. MF-0.1 achieves the highest volumetric capacitance of 1239 F cm^{-3} at 5 mV s^{-1}, which is comparable to previously reported $Ti_3C_2T_x$ films (Fig. 3(b)) [54]. Interestingly, all samples exhibit similar capacitance retention ability as scan rates increase (Fig. S10 in the ESM). This suggests a performance trade-off between electronic conduction and ionic transport. The compact, highly conductive MF-0.1 fiber ensures efficient electron transport, whereas the looser structure of other fibers made with higher Fe^{2+} concentrations facilitates better electrolyte infiltration and faster ion access.

Electrochemical kinetic analysis using the power-law relationship $i = av^b$ (where i and v are the peak current and scan rate, respectively) was performed to distinguish between capacitive and diffusion-controlled processes [55]. The calculated b values were between 0.71 and 0.83 for all fibers (Fig. 3(c)). Further quantitative analysis of the contribution ratios of surface-controlled and diffusion-controlled processes was performed using the formula $i(V)=k_1v+k_2v^{1/2}$, where k_1v and $k_2v^{1/2}$ corresponds to the capacitive-controlled and diffusion-controlled current, respectively (Fig. S11) [56]. As the scan rate increases, the capacitive-controlled contribution ratio gradually rises, which increases from 41.71% at 5 mV s^{-1} to 68.27% at 50 mV s^{-1} for MF-0.1. This fitting result demonstrates a hybrid energy storage mechanism, incorporating both surface-controlled capacitive reaction and diffusion-controlled intercalation process [57]. This dual-mechanism characteristic stems from the unique surface and internal wrinkled textures as well as the chemical properties of the fibers: 1) The highly wrinkled surface provides abundant active sites for rapid surface pseudocapacitive reactions, promoting capacitive-controlled kinetics; 2) The open porous structure effectively prevents the dense "face-to-face" stacking of MXene nanosheets to form abound of ion channels, to enable the diffusion-controlled ion intercalation behavior [51,53].

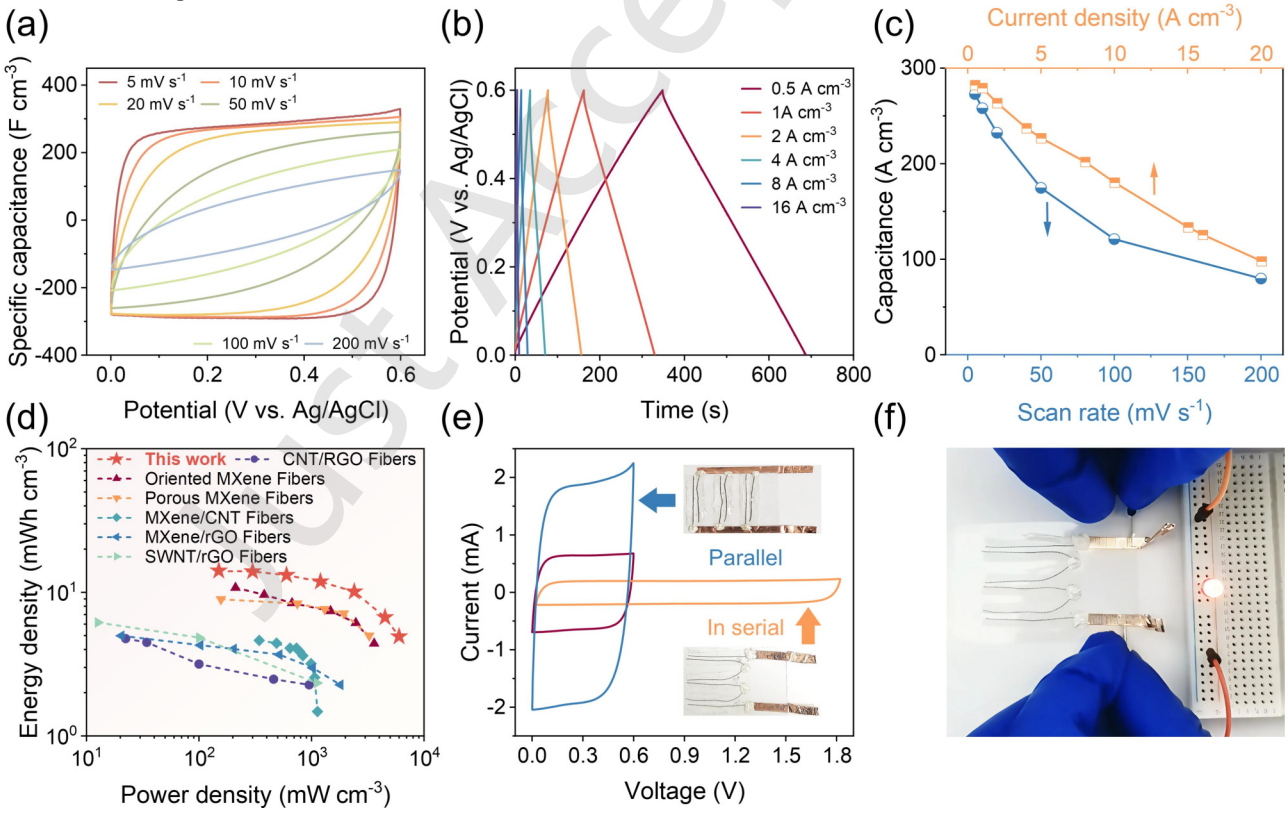

Figure 4. Electrochemical performance of MF-0.1 fiber-based supercapacitor and prototype for practical power applications. (a) CV curves at various scan rates. (b) GCD curves at various current densities. (c) Volumetric capacitance versus scan rates and current densities. (d) Ragone plots comparing energy and power densities with literature values for fiber-based supercapacitors [28,44,58-61]. (e) CV curves of series- and parallel-connected FSCs (photos inset). (f) Optical image demonstrating a red LED powered by three series-connected FSCs.

In addition, the galvanostatic charge-discharge (GCD) curves exhibit highly symmetric triangular profiles under different current densities (see Fig. 3(d) and S12 in the ESM), with a tiny *IR* drop, indicating the excellent coulombic efficiency. Electrochemical impedance spectroscopy (EIS) further probed the charge transfer and ion transport kinetics of the fibers (Fig. 3(e)). The near-vertical behavior in the low-frequency region, small equivalent series resistance (ESR, <0.1 Ω cm^3) and

negligible Warburg region evidence their good capacitive behavior and efficient ion diffusion within the electrode structure. These findings, particularly the rapid ion diffusion kinetics indicated by the vertical slope, are in excellent agreement with the results of the above power-law analysis, confirming that the optimized fiber structure facilitates efficient ion transport.

The charge-discharge cycling stability of MF-0.1 fiber was further evaluated over 10,000 CV cycles at 100 mV s^{-1}. Remarkably, the specific capacitance keeps increasing during the overall test, reaching ~115% of its initial value, with negligible deviations in the CV curve shape (Fig. 3(f)). This increase in capacitance could be attributed to an electrochemical activation process driven by electro-wetting effect, which involves continuous ion intercalation that gradually expands the interlayer spacing and improves electrolyte infiltration into the deep, compact interlayers of the fiber. Crucially, the unique wrinkled surface texture of the fiber facilitates this process by providing non-densified surface channels that act as initial pathways for electrolyte ingress. These structural and interfacial changes, combined with the gradual wetting of previously inaccessible internal surfaces, collectively activate more redox-active sites for charge storage. Notably, such exceptional stability and performance enhancement are closely associated with the robust Fe^{2+}-crosslinking wrinkled texture framework, which effectively stabilizes the architecture by acting as a mechanical buffer layer that mitigates structural degradation under prolonged electrochemical cycling [22,51,62]. These results underscore the critical role of Fe^{2+}-mediated structural engineering in achieving high electrochemical durability and offer valuable insights for designing advanced MXene-based fiber electrodes.

To demonstrate their practical viability, two MF-0.1 fibers were assembled in parallel to fabricate a quasi-solid-state fiber-shaped supercapacitor (FSC), using PVA-H_2SO_4 gel electrolyte (Fig. S13 in the ESM). The CV curves reveal a typical pseudocapacitive shape within a stable voltage window of 0-0.6 V, which maintains quasi-rectangular profiles even at a high scan rate of 200 mV s^{-1}, indicating rapid charge transfer kinetics (Fig. 4(a)). The GCD curves exhibit nearly symmetrical triangular profiles across a range of current densities, confirming efficient charge/discharge behavior and low internal resistance (Fig. 4(b)). The volumetric capacitance was further calculated based on both CV and GCD data, reaching 273 F cm^{-3} at 5 mV s^{-1} and 282 F cm^{-3} at 0.5 A cm^{-3}, respectively (Fig. 4(c)). The device also exhibits excellent rate capability, retaining 80 F cm^{-3} even at 200 mV s^{-1}, which is crucial for applications requiring rapid power delivery. In addition, the FSC demonstrates good cycling stability, retaining over 80% of its initial capacitance after 1,000 charge-discharge cycles (see Fig. S14 in the ESM).

As shown in Fig. 4(d), the Ragone plot compares the volumetric energy density (E_V) and power density (P_V) with previously reported fiber-based supercapacitors, highlighting the superior performance of the FSC. The device achieves a maximum E_V of 14.12 mWh cm^{-3} at a P_V of 149.91 mW cm^{-3}, while maintaining 4.92 mWh cm^{-3} even at an ultrahigh P_V of 6000.41 mW cm^{-3}. These performance metrics surpass those of most previously reported fiber-based supercapacitors, benefiting from the high intrinsic conductivity of $Ti_3C_2T_x$ and the optimized ion/electron transport pathways enabled by the Fe^{2+}-crosslinked structure [28,44,58-61].

To assess their potential for practical applications, the FSCs were connected in series and parallel to increase the output voltage and current, thereby adapting to the requirements of appliances and confirming their excellent circuit compatibility and scalable electrical behavior (Fig. 4(e)). As a demonstration, three FSCs connected in series can extend the output voltage to 1.8 V and successfully power a commercial red light-emitting diode (Fig. 4(f)). The combination of high capacitance, customizable output characteristics, inherent flexibility, and potential weavability positions these fibers as promising miniaturized energy solutions for next-generation flexible and wearable electronic systems.

2.4 Electrothermal and Electromagnetic Interference Shielding

The exceptionally high electrical conductivity may endow the MF-0.1 fiber with good Joule heating and electromagnetic interference (EMI) shielding effects. Combined with its robust mechanical flexibility and weavability, the fiber exhibits great potential toward wearable e-textiles for personal thermal management and electromagnetic protection [63,64]. As shown in Fig. 5(a), a 1 cm-long MF-0.1 fiber segment was bridged between two copper electrodes and powered by direct-current voltage. The voltage-dependent temperature was monitored via an infrared thermography camera. Under an applied voltage of 2.0 V, the fiber's surface temperature increased from ambient (~25°C) to a steady-state value of 122°C within 2 min, yielding an average heating efficiency of $\Delta T/V$ = 48.5°C V^{-1} (Fig. 5(b)). As for the application of personal thermal management, relatively lower temperatures are more desirable. Reassuringly, under a low driving voltage of 1.5 V, the fiber can rapidly reach comfortable temperatures for the human body, attaining 35°C in just 15 seconds and 45°C in 110 seconds, which satisfies the basic requirements for basic warmth and targeted thermotherapy while ensuring both user safety and energy efficiency. As detailed in Table S2 in the ESM, its low-voltage operation ability is highly competitive with other reported fiber-based heaters, making it highly beneficial for ensuring the safety of wearable electronic devices.

The inherent weavability of the fiber allows for the construction of complex conductive patterns for tailored heating applications. As shown in Fig. 5(c), three bent fiber segments (1 cm length each) were connected to form a "smiley face" heater, which shows homogeneous temperature distribution under infrared thermography at 6 V. This combination of low-voltage operation, rapid thermal response, customizable patternability, and mechanical

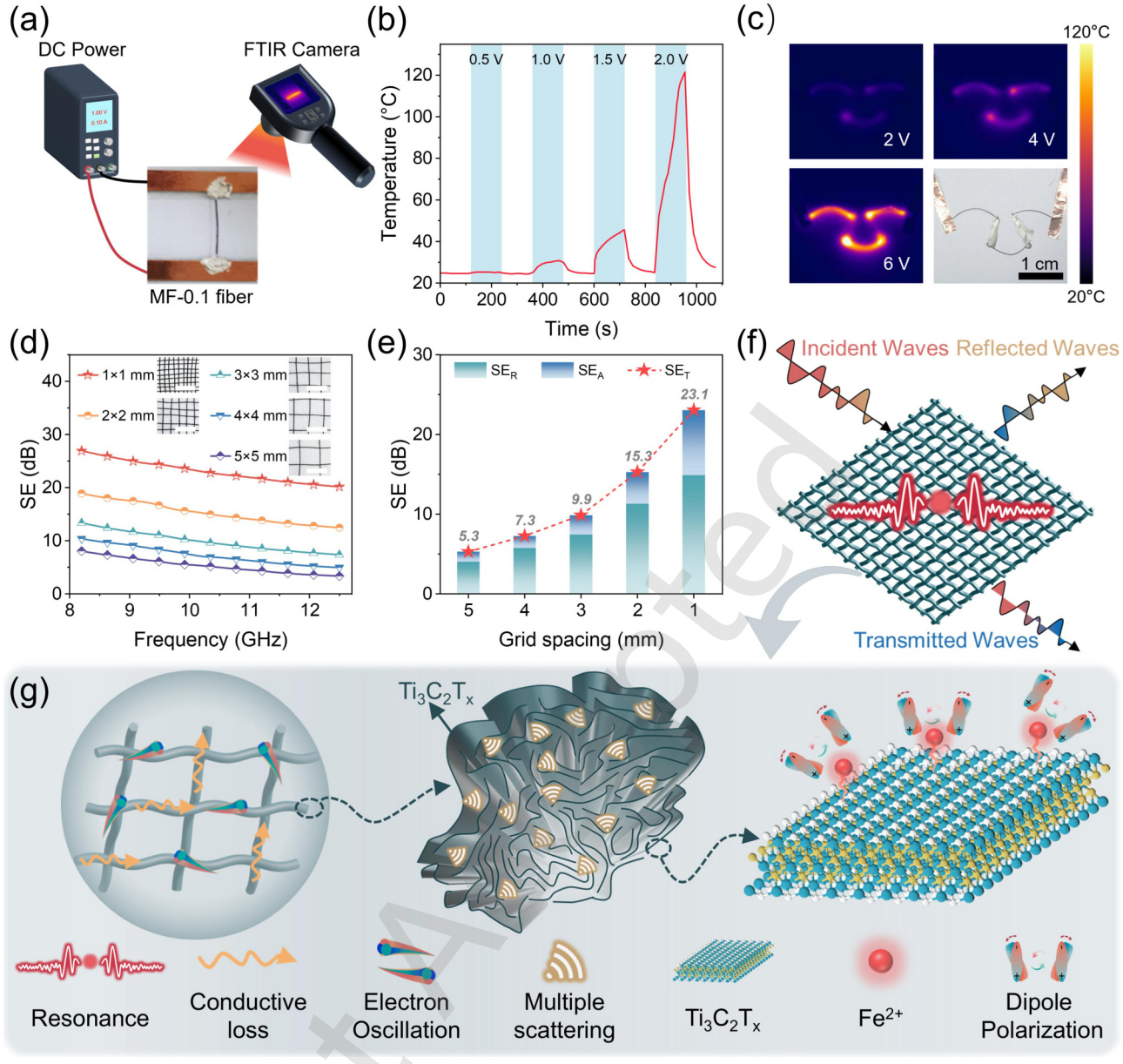

Figure 5. Electrothermal and EMI shielding applications of MF-0.1 fibers. (a) Schematic of the electrothermal testing setup. (b) Temperature versus time profiles under different applied voltages. (c) Infrared thermal image of a "smiley face" pattern heater at various voltages. (d) EMI SE spectra of textiles with varying grid spacings in the X-band; the inset displays photographs of the corresponding textile grids (scale bar: 5 cm). (e) Comparison of average SE_T, SE_A, and SE_R values for different grid configurations. (f) Schematic illustrating the EMI shielding mechanism by the MF-X fiber grid. (g) Conceptual multiscale analysis of electromagnetic attenuation mechanisms within the Fe^{2+}-crosslinked $Ti_3C_2T_x$ fiber structure.

flexibility provides a strong foundation for developing personalized thermotherapy systems and intelligent thermal-regulating textiles.

On the other hand, the highly conductive MF-0.1 fiber is an ideal candidate for comfortable EMI shielding textiles toward the humanbody electromagnetic protection [65]. To determine the optimal weave density, the MF-0.1 fibers were woven into grids with spacing varying from 1 mm to 5 mm, whose EMI shielding effectiveness (SE) were systematically evaluated in the X-band (8.2-12.5 GHz). As shown in Fig. 5(d), the total SE (SE_T) value is enhanced from 5.3 dB to 23.1 dB, as the grid spacing is reduced from 5 mm to 1 mm, corresponding to a significant improvement in shielding efficiency from ~70% to ~99.5% of the incident electromagnetic power. Notably, the SE value shows an obvious sharp rise when the grid spacing is narrower than 3 mm. Current research on MXene fiber-based shielding textiles mainly focuses on MXene-based composite fibers. The additive-free pure MXene fibers have rarely been reported for application in woven grid-type EMI shielding textiles due to their relatively weak mechanical strength. Benefiting from the enhanced mechanical strength and excellent electrical conductivity induced by Fe^{2+}-crosslinking, this study has realized the application of pure MXene fibers in woven shielding textiles. Although the EMI SE value of this fabric is not the most prominent among the reported MXene-based textiles (Table S3), it has fully met the standard shielding requirement for commercial applications (20 dB) and possesses practical application potential [66]. In addition, the EMI shielding ability could also be further enhanced by increasing the weaving density. As shown in Fig. 5(e), reflection is the primary contributor to EMI attenuation, with reflection effectiveness (SE_R) dominating over absorption effectiveness (SE_A) across all grid configurations. Critically, both SE_R and SE_A increase as the grid spacing is reduced. This trend underscores a key advantage

of the woven architecture: a denser conductive network not only enhances wave reflection by intensifying the impedance mismatch but also simultaneously improves the textile's intrinsic capacity for energy absorption and dissipation.

The reflection-dominant behavior is attributed to the high concentration of mobile charge carriers in the metallic $Ti_3C_2T_x$, which creates a significant impedance mismatch at the air-textile interface, leading to the reflection of a large portion of incident electromagnetic waves (EMWs) [67]. The overall shielding performance, however, arises from synergistic effects across multiple scales. At the macroscopic level, increasing the grid density intensifies the collective impedance mismatch of the conductive network, leading to stronger reflection of EMWs. Concurrently, the periodic grid architecture can enhance energy dissipation through mechanisms like scattering within the network, contributing to the absorption component (Fig. 5(f)) [68]. At the microscopic level within each fiber, the percolation networks formed by the highly conductive, Fe^{2+}-crosslinked $Ti_3C_2T_x$ nanosheets dissipate electromagnetic energy via conductive loss and collective electron oscillations (Fig. 5(g)) [69]. The unique cylindrical geometry and helically stacked arrangement of the nanosheets within the fiber, compared to the planar stacking in conventional films, may provide additional scattering surfaces that further augment internal reflections, contributing to enhanced energy dissipation [70,71]. Finally, at the nanoscale, the Fe^{2+}-induced interfacial charge redistribution may create localized dipole polarization and dielectric relaxation [72,73], further contributing to energy absorption.

The performance of the woven textile underscores the distinct advantages of our material and structural design. Fe^{2+}-crosslinking not only significantly enhances the mechanical strength and flexibility of the fibers, thereby conferring weavability, but also preserves high electrical conductivity for EMI shielding. This woven architecture provides excellent adjustable shielding effectiveness while offering critical advantages for wearable applications, such as lightweight comfort, breathability, and flexibility, which are unattainable with the dense solid films that usually achieve higher absolute shielding. By integrating atomic-scale interfacial engineering (Fe^{2+}-crosslinking) with macroscopic structural design (textile weaving), this work leverages both dominant reflection and supplementary absorption mechanisms to create high-performance, intelligent electromagnetic protective textiles for next-generation wearable systems.

3 Conclusion

In summary, the Fe^{2+}-crosslinking dynamic assembly strategy was demonstrated for the wet-spinning of multifunctional $Ti_3C_2T_x$ MXene fibers. The coordination bridging between Fe^{2+} ions and $Ti_3C_2T_x$ layers effectively reinforces interlayer bonding, which stabilizes the highly oriented alignment of nanosheets within the fibers. This engineered architecture endows the fibers with an exceptional combination of mechanical strength (143.7 MPa) and electrical conductivity (2607 S cm^{-1}), thus enabling exceptional performance across multiple applications. The fibers show a superior pseudocapacitive charge storage capacity of 1239 F cm^{-3}, enabling fiber-shaped supercapacitors with a high energy density of 14.12 mWh cm^{-3} and a power density of 6000.41 mW cm^{-3}. Furthermore, their high conductivity allows for efficient Joule heating (48.5°C V^{-1}) and tunable EMI shielding (up to 23.1 dB) when woven into textiles. This work underscores the efficacy of interfacial engineering via ionic crosslinking for developing high-performance MXene fibers, offering a versatile platform for next-generation wearable electronics.

4 Method section

4.1 Materials

Ti_3AlC_2 (400 mesh) was purchased from Jilin 11 Technology Co., Ltd. Concentrated hydrochloric acid (HCl, 36.5%-38%) and ferrous chloride tetrahydrate ($FeCl_2·4H_2O$, 99%) were supplied by Shanghai Sinopharm Group Chemical Reagent Co., Ltd. Lithium fluoride (LiF, 99%) was sourced from Jinan Maina Technology Co. The resistance of deionized (DI) water was ~18 MΩ cm.

4.2 Fabrication of $Ti_3C_2T_x$ MXene

45 mL of concentrated HCl was added to 15 mL of DI water in a polytetrafluoroethylene reaction flask. Then, 4.8 g of LiF was added and stirred at 600 rpm for 5 min until dissolved. Subsequently, 3.0 g of Ti_3AlC_2 MAX powder was slowly added to the mixed solution while stirring. The mixture was maintained at 35°C for 24 hours under continuous stirring. After etching, the solution was diluted with DI water and centrifuged at 3500 rpm for 5min. The supernatant was discarded, and this washing/centrifugation process was repeated until the supernatant pH approached 6. The resulting precipitate was then redispersed in DI water and centrifuged at 3500 rpm for 3 min. The upper supernatant layer containing delaminated monolayer $Ti_3C_2T_x$ dispersion was collected.

4.3 Preparation of Spinning Solutions

An appropriate amount of $Ti_3C_2T_x$ MXene aqueous solution was centrifuged at 11000 rpm for 20 min. The supernatant was removed, and the highly concentrated monolayer $Ti_3C_2T_x$ MXene slurry deposited at the bottom was collected. Then, the monolayer $Ti_3C_2T_x$ MXene spinning solutions with different concentrations (40, 60, 80, 100, and 120 mg mL^{-1}) were prepared by adding calculated amounts of DI water to dilute the concentrated slurry.

4.4 Preparation of $FeCl_2$ Coagulation Bath

Appropriate amounts of solid $FeCl_2·4H_2O$ particles were added to DI water and stirred until complete dissolution. Coagulation baths of $FeCl_2$ with concentrations of 0.1 mol/L, 0.2 mol/L, 0.3 mol/L, 0.4 mol/L, and 0.5 mol/L were prepared separately.

4.5 Preparation of $Ti_3C_2T_x$ MXene Fibers

MXene fibers were prepared via wet spinning using a custom-built spinning apparatus (as illustrated in Fig. 1(a)). A specific concentration of $Ti_3C_2T_x$ spinning solution was loaded into a syringe connected to a spinning nozzle (0.5 mm inner diameter). A syringe pump extruded the solution at a controlled rate into the rotating coagulation bath containing the $FeCl_2$ solution. The nematically arranged $Ti_3C_2T_x$ liquid crystals underwent Fe^{2+} complexation and solidification upon contact with the bath, forming continuous fibers. The fiber formation process is visualized in Movie S1. After ~5 min of immersion, the fibers were collected using a rotating spool. Finally, the obtained fibers were dried at room temperature and stored in a vacuum drying oven.

4.6 Demonstration Cases for Power Supply and Joule Heating

Silver paste was employed at all fiber junctions and terminal connections to ensure mechanical stability and minimize contact resistance, ensuring the accuracy of the electrothermal and circuit demonstrations. For the LED demonstration in Fig. 4f, three FSC units were connected in series via silver paste. For the 'smiley face' heater in Fig. 5c, the bent fibers were fixed onto the paper substrate and electrically connected to the circuit using silver paste, ensuring both mechanical adhesion and electrical continuity during operation.

4.7 Characterizations and Measurements

The liquid crystal orientation of $Ti_3C_2T_x$ solutions was observed using a polarizing optical microscope (POM, Eclipse Ci POL, Nikon). The surface and cross-sectional morphology of fibers were observed using a field emission scanning electron microscope (FE-SEM, S4800, HITACHI). XRD patterns were recorded using an X-ray diffractometer (D8 Advance A25). The rheological properties of $Ti_3C_2T_x$ dispersion were measured using a rheometer (Discovery HR 30) under dynamic oscillation conditions. The stress-strain characteristics of $Ti_3C_2T_x$ fibers were tested via a universal electronic material testing machine (Instron 3365). Infrared thermography images were captured using an infrared camera (FLIR E40).

Due to the irregular cross-sections of the fibers, direct measurement of volume and diameter is unfeasible. Multiple cross-sectional SEM images (≥3 positions per sample) were therefore captured, and the average cross-sectional area (S) was determined via ImageJ software. The volume (V) was calculated as $V = S \times h$ (h denotes the fiber length), and the equivalent diameter (d) was calculated using the circular area-diameter formula ($S = \pi d^2/4$).

4.8 Electrochemical properties of $Ti_3C_2T_x$ fibers

Electrochemical measurements were performed using a three-electrode setup in 1 M H_2SO_4 electrolyte with an electrochemical workstation (Corrtest CS310H). MF-X fibers served as the working electrode, an activated carbon film as the counter electrode, and Ag/AgCl as the reference electrode. Cyclic voltammetry (CV), galvanostatic charge-discharge (GCD), and electrochemical impedance spectroscopy (EIS) were conducted. EIS measurements were carried out at open circuit potential, using an alternating current (AC) voltage amplitude of 10 mV and a frequency range of 1 MHz to 10 mHz. Cycling stability was assessed via CV at 100 mV s^{-1} for 10,000 cycles. For the three-electrode setup, current and current density in the CV and GCD curves were normalized by the active material volume.

Volumetric specific capacitance (C_V) from CV curves was calculated according to Eq. (1):

$$C_V = \frac{\int IdU}{Vv\Delta U} \#(1)$$

where I is the current (A), v is the scan rate (V s^{-1}), ΔU is the voltage window (V), and V is the volume of the fiber electrode (cm^3).

Capacitance retention rate (C_r) was calculated using Eq. (2):

$$C_r = \frac{C_i}{C_1} \#(2)$$

where C_i and C_1 are the specific capacitances at the i-th and first cycles, respectively.

4.9 Electrochemical tests of fiber-shaped supercapacitors

For the symmetric two-electrode FSC device, the capacitance (C_D) was calculated from the CV and GCD curves according to Eq. (3) and (4), respectively:

$$C_D = \frac{\int IdU}{2v\Delta U} \#(3)$$

$$C_D = \frac{it_{dis}}{\Delta U - U_{IR}} \#(4)$$

where i is the discharge current (A), t_{dis} is the discharge time (s), and U_{IR} is the voltage drop at the beginning of the discharge on the GCD discharge curve.

The volumetric energy density (E_V) and volumetric power density (P_V) of the fiber-shaped supercapacitors were calculated from the GCD curves according to Eq. (5) and (6):

$$E_V = \frac{1}{2} C_D (\Delta U - U_{IR})^2 \#(5)$$

$$P_V = \frac{E}{t_{dis}} \#(6)$$

4.10 EMI Shielding Measurements

EMI SE was measured using a vector network analyzer (VNA) in the X-band (8.2-12.5 GHz) with a waveguide sample holder. Total shielding effectiveness SE_T is the sum of absorption SE_A and reflection effectiveness SE_R, as Eq. (7):

$$SE_T = SE_R + SE_A \#(7)$$

Reflection (R), transmission (T), and absorption (A) coefficients are calculated from scattering parameters S_{11} and S_{21} using Eq. (8)-(10):

$$R = |S_{11}|^2 \#(8)$$

$$T = |S_{21}|^2 \#(9)$$

$$A = 1 - R - T \#(10)$$

And SE_R, SE_A, and SE_T are calculated using Eq. (11)-(13):

$$SE_R = 10\log_{10}\left(\frac{1}{1-R}\right) = 10\log_{10}\left(\frac{1}{1-|S_{11}|^2}\right) \#(11)$$

$$SE_A = 10\log_{10}\left(\frac{1-R}{T}\right) = 10\log_{10}\left(\frac{1-|S_{11}|^2}{|S_{21}|^2}\right) \#(12)$$

$$SE_T = SE_R + SE_A = 10\log_{10}\left(\frac{1}{T}\right) = 10\log_{10}\left(\frac{1}{|S_{21}|^2}\right) \#(13)$$

Electronic Supplementary Material: Supplementary material (please provide the brief detail of the ESM) is available in the online version of this article at https://doi.org/10.26599/NR.2026.94908426.

Data availability

All data needed to support the conclusions in the paper are presented in the manuscript and/or the Electronic Supplementary Material. Additional data related to this paper may be requested from the corresponding author upon request.

Acknowledgements

This work is granted by the National Natural Science Foundation of China (Grant No. 22105106), the Natural Science Foundation of Jiangsu Province of China (Grant No. BK20210603), the Jiangsu Youth Science and Technology Talent Support Program (Grant No. JSTJ-2025-063), Nanjing

Science and Technology Innovation Project for Overseas Students (Grant No. NJKCZYZZ2022-05), Start-up Funding from NUPTSF (Grant No. NY221003), and Postgraduate Research & Practice Innovation Program of Jiangsu Province (KYCX24_1171).

Declaration of competing interest

All the contributing author(s) report(s) no conflict of interests in this work.

Author contribution statement

W. Fei: data curation, formal analysis, funding acquisition, investigation, methodology, visualization, writing – original draft; X. Wang: data curation, formal analysis, investigation, visualization, writing – original draft; C. Miao: data curation, formal analysis, investigation, methodology, visualization, writing – original draft; J. Chen: investigation, methodology; S. Liu: resources, supervision; B. Li: formal analysis, resources, writing – review & editing; Jianmin Li: conceptualization, funding acquisition, project administration, supervision, writing – review & editing; Qiang Zhao: resources, supervision. All the authors have approved the final manuscript."

Informed consent

Not applicable.

Ethics statement

Not applicable.

Use of AI statement

During the preparation of this work, the authors used Google Gemini in order to refine text and check grammar. After using this tool/service, the authors reviewed and edited the content as needed and take full responsibility for the content of the publication

References

[1] Rogers, J. A.;Someya, T.; Huang, Y. Materials and mechanics for stretchable electronics. *Science* **2010**, *327*, 1603-1607.

[2] Shi, H. H.;Pan, Y.;Xu, L.;Feng, X.;Wang, W.;Potluri, P.;Hu, L.;Hasan, T.; Huang, Y. Y. S. Sustainable electronic textiles towards scalable commercialization. *Nat. Mater.* **2023**, *22*, 1294-1303.

[3] Son, D.;Lee, J.;Qiao, S.;Ghaffari, R.;Kim, J.;Lee, J. E.;Song, C.;Kim, S. J.;Lee, D. J.; Jun, S. W. Multifunctional wearable devices for diagnosis and therapy of movement disorders. *Nat. Nanotechnol.* **2014**, *9*, 397-404.

[4] Ding, Y.;Jiang, J.;Wu, Y.;Zhang, Y.;Zhou, J.;Zhang, Y.;Huang, Q.; Zheng, Z. Porous conductive textiles for wearable electronics. *Chem. Rev.* **2024**, *124*, 1535-1648.

[5] Shen, D.;Xiao, M.;Zou, G.;Liu, L.;Duley, W. W.; Zhou, Y. N. Wearable Electronics: Self‐Powered Wearable Electronics Based on Moisture Enabled Electricity Generation. *Adv. Mater.* **2018**, *30*, 1870128.

[6] Kim, D.;Lu, N.;Ma, R.;Kim, Y.;Kim, R.;Wang, S.;Wu, J.;Won, S. M.;Tao, H.; Islam, A. Epidermal electronics. *Science* **2011**, *333*, 838-843.

[7] Xu, S.;Zhang, Y.;Jia, L.;Mathewson, K. E.;Jang, K.;Kim, J.;Fu, H.;Huang, X.;Chava, P.; Wang, R. Soft microfluidic assemblies of sensors, circuits, and radios for the skin. *Science* **2014**, *344*, 70-74.

[8] Fan, F. R.;Tang, W.; Wang, Z. L. Flexible nanogenerators for energy harvesting and self‐powered electronics. *Adv. Mater.* **2016**, *28*, 4283-4305.

[9] Chen, G.;Xiao, X.;Zhao, X.;Tat, T.;Bick, M.; Chen, J. Electronic textiles for wearable point-of-care systems. *Chem. Rev.* **2022**, *122*, 3259-3291.

[10] Inman, A.;Parker, T.;Zhang, Y.;Saraf, M.; Gogotsi, Y. Obtaining a Practical Wearable Supercapacitor Power Supply. *Adv. Energy Mater.* **2024**, *14*, 2402367.

[11] Hu, H.;Shang, S.;Liu, J.; Zhu, P. Silk fibroin based flexible and self-powered sensor for real-time monitoring of abdominal respiration. *Int. J. Biol. Macromol.* **2024**, *254*, 127723.

[12] Shi, J.;Liu, S.;Zhang, L.;Yang, B.;Shu, L.;Yang, Y.;Ren, M.;Wang, Y.;Chen, J.; Chen, W. Smart textile‐integrated microelectronic systems for wearable applications. *Adv. Mater.* **2020**, *32*, 1901958.

[13] Won, D.;Bang, J.;Choi, S. H.;Pyun, K. R.;Jeong, S.;Lee, Y.; Ko, S. H. Transparent electronics for wearable electronics application. *Chem. Rev.* **2023**, *123*, 9982-10078.

[14] Xiong, J.;Chen, J.; Lee, P. S. Functional fibers and fabrics for soft robotics, wearables, and human–robot interface. *Adv. Mater.* **2021**, *33*, 2002640.

[15] Wang, M. C.;Zhang, X.;Majidi, E.;Nedelec, K.; Gates, B. D. Electrokinetic assembly of selenium and silver nanowires into macroscopic fibers. *ACS Nano* **2010**, *4*, 2607-2614.

[16] Jang, Y.;Kim, S. M.;Spinks, G. M.; Kim, S. J. Carbon nanotube yarn for fiber‐shaped electrical sensors, actuators, and energy storage for smart systems. *Adv. Mater.* **2020**, *32*, 1902670.

[17] Liu, Y.; Kumar, S. Polymer/carbon nanotube nano composite fibers–a review. *ACS Appl. Mater. Interfaces* **2014**, *6*, 6069-6087.

[18] Matsuhisa, N.;Chen, X.;Bao, Z.; Someya, T. Materials and structural designs of stretchable conductors. *Chem. Soc. Rev.* **2019**, *48*, 2946-2966.

[19] Eom, W.;Shin, H.;Ambade, R. B.;Lee, S. H.;Lee, K. H.;Kang, D. J.; Han, T. H. Large-scale wet-spinning of highly electroconductive MXene fibers. *Nat. Commun.* **2020**, *11*, 2825.

[20] Zhou, Y.;Zhang, Y.;Ruan, K.;Guo, H.;He, M.;Qiu, H.; Gu, J. MXene-based fibers: preparation, applications, and prospects. *Sci. Bull.* **2024**, *69*, 2776-2792.

[21] Hantanasirisakul, K.; Gogotsi, Y. Electronic and optical properties of 2D transition metal carbides and nitrides (MXenes). *Adv. Mater.* **2018**, *30*, 1804779.

[22] Zhang, J.;Uzun, S.;Seyedin, S.;Lynch, P. A.;Akuzum, B.;Wang, Z.;Qin, S.;Alhabeb, M.;Shuck, C. E.; Lei, W. Additive-free MXene liquid crystals and fibers. *ACS Cent. Sci.* **2020**, *6*, 254-265.

[23] Wang, H.;Wang, Y.;Chang, J.;Yang, J.;Dai, H.;Xia, Z.;Hui, Z.;Wang, R.;Huang, W.; Sun, G. Nacre-inspired strong MXene/cellulose fiber with superior supercapacitive performance via synergizing the interfacial bonding and interlayer spacing. *Nano Lett.* **2023**, *23*, 5663-5672.

[24] Liu, L.;Chen, W.;Zhang, H.;Ye, L.;Wang, Z.;Zhang, Y.;Min, P.; Yu, Z. Super-tough and environmentally stable aramid. Nanofiber@ MXene coaxial fibers with outstanding electromagnetic interference shielding efficiency. *Nano-Micro Lett.* **2022**, *14*, 111.

[25] Wan, S.;Li, X.;Chen, Y.;Liu, N.;Du, Y.;Dou, S.;Jiang, L.; Cheng, Q. High-strength scalable MXene films through bridging-induced densification. *Science* **2021**, *374*, 96-99.

[26] Wan, S.;Chen, Y.;Huang, C.;Huang, Z.;Liang, C.;Deng, X.; Cheng, Q. Scalable ultrastrong MXene films with superior osteogenesis. *Nature* **2024**, *634*, 1103-1110.

[27] Dai, H.;Chang, J.;Yang, J.;Wang, H.;Zhou, J.; Sun, G. Bio‐Inspired Interfacial Engineering of MXene Fibers Toward Synergistic Improvement in Mechanical Strength and Electrochemical Performance. *Adv. Funct. Mater.* **2024**, *34*, 2312654.

[28] Li, S.;Fan, Z.;Wu, G.;Shao, Y.;Xia, Z.;Wei, C.;Shen, F.;Tong, X.;Yu, J.; Chen, K. Assembly of nanofluidic MXene fibers with enhanced ionic transport and capacitive charge storage by flake orientation. *ACS Nano* **2021**, *15*, 7821-7832.

[29] Deng, Y.;Shang, T.;Wu, Z.;Tao, Y.;Luo, C.;Liang, J.;Han, D.;Lyu, R.;Qi, C.; Lv, W. Fast gelation of Ti3C2Tx MXene initiated by metal ions. *Adv. Mater.* **2019**, *31*, 1902432.

[30] Zhou, X.;Wen, J.;Ma, X.; Wu, H. Manipulation of microstructure of MXene aerogel via metal ions-initiated gelation for electromagnetic wave absorption. *J. Colloid Interface Sci.* **2022**, *624*, 505-514.

[31] Lipatov, A.;Alhabeb, M.;Lukatskaya, M. R.;Boson, A.;Gogotsi, Y.; Sinitskii, A. Effect of synthesis on quality, electronic properties and environmental stability of individual monolayer Ti3C2 MXene flakes. *Adv.*

Electron. Mater. **2016**, *2*, 1600255.

[32] Onsager, L. The effects of shape on the interaction of colloidal particles. *Ann. N. Y. Acad. Sci.* **1949**, *51*, 627-659.

[33] Guo, F.;Kim, F.;Han, T. H.;Shenoy, V. B.;Huang, J.; Hurt, R. H. Hydration-responsive folding and unfolding in graphene oxide liquid crystal phases. *ACS Nano* **2011**, *5*, 8019-8025.

[34] Li, H.;Shao, F.;Wen, X.;Ding, Y.;Zhou, C.;Zhang, Y.;Wei, H.; Hu, N. Graphene/MXene fibers-enveloped sulfur cathodes for high-performance Li-S batteries. *Electrochim. Acta* **2021**, *371*, 137838.

[35] Zhang, J.;Kong, N.;Uzun, S.;Levitt, A.;Seyedin, S.;Lynch, P. A.;Qin, S.;Han, M.;Yang, W.; Liu, J. Scalable manufacturing of free-standing, strong Ti3C2Tx MXene films with outstanding conductivity. *Adv. Mater.* **2020**, *32*, 2001093.

[36] Liu, J.;Qing, Y. M.;Wu, J. J.;Tian, J. Q.;Feng, C. B.;Zhou, X. Y.;Ma, Y.;Li, B. X.;Lu, Y. Q.; Li, Q. Responsive cellulose nanocrystal‐based liquid crystals: From structural color manipulation to applications. *Responsive Mater.* **2025**, *3*, e70020.

[37] Xu, T.;Du, H.;Liu, H.;Liu, W.;Zhang, X.;Si, C.;Liu, P.; Zhang, K. Advanced nanocellulose‐based composites for flexible functional energy storage devices. *Adv. Mater.* **2021**, *33*, 2101368.

[38] Cong, H.;Ren, X.;Wang, P.; Yu, S. Wet-spinning assembly of continuous, neat and macroscopic graphene fibers. *Sci. Rep.* **2012**, *2*, 613.

[39] Eklöf-Österberg, J.;Löfgren, J.;Erhart, P.; Moth-Poulsen, K. Understanding interactions driving the template-directed self-assembly of colloidal nanoparticles at surfaces. *J. Phys. Chem. C* **2020**, *124*, 4660-4667.

[40] Cao, X.;Wu, G.;Li, K.;Hou, C.;Li, Y.;Zhang, Q.; Wang, H. High‐Performance Zn2+‐Crosslinked MXene Fibers for Versatile Flexible Electronics. *Adv. Funct. Mater.* **2024**, *34*, 2407975.

[41] Wang, Z.;Qin, S.;Seyedin, S.;Zhang, J.;Wang, J.;Levitt, A.;Li, N.;Haines, C.;Ovalle-Robles, R.; Lei, W. High‐performance biscrolled MXene/carbon nanotube yarn supercapacitors. *Small* **2018**, *14*, 1802225.

[42] Zhang, J.;Seyedin, S.;Qin, S.;Wang, Z.;Moradi, S.;Yang, F.;Lynch, P. A.;Yang, W.;Liu, J.; Wang, X. Highly conductive Ti3C2Tx MXene hybrid fibers for flexible and elastic fiber‐shaped supercapacitors. *Small* **2019**, *15*, 1804732.

[43] Yang, Q.;Xu, Z.;Fang, B.;Huang, T.;Cai, S.;Chen, H.;Liu, Y.;Gopalsamy, K.;Gao, W.; Gao, C. MXene/graphene hybrid fibers for high performance flexible supercapacitors. *J. Mater. Chem. A* **2017**, *5*, 22113-22119.

[44] Seyedin, S.;Yanza, E. R. S.; Razal, J. M. Knittable energy storing fiber with high volumetric performance made from predominantly MXene nanosheets. *J. Mater. Chem. A* **2017**, *5*, 24076-24082.

[45] Zhu, C.; Geng, F. Macroscopic MXene ribbon with oriented sheet stacking for high‐performance flexible supercapacitors. *Carbon Energy* **2021**, *3*, 142-152.

[46] Tang, Z.;Kotov, N. A.;Magonov, S.; Ozturk, B. Nanostructured artificial nacre. *Nat. Mater.* **2003**, *2*, 413-418.

[47] Gong, L.;Kinloch, I. A.;Young, R. J.;Riaz, I.;Jalil, R.; Novoselov, K. S. Interfacial stress transfer in a graphene monolayer nanocomposite. *Adv. Mater.* **2010**, *22*, 2694–2697.

[48] Shang, S.;Zheng, Y.;Wei, L.;Liu, J.; Zhu, P. Preparation of strong and tough alginate fibers through multiple Ca2+ crosslinking structures and interpenetrating networks. *Int. J. Biol. Macromol.* **2025**, *322*, 146726.

[49] Gong, L.;Kinloch, I. A.;Young, R. J.;Riaz, I.;Jalil, R.; Novoselov, K. S. Interfacial stress transfer in a graphene monolayer nanocomposite. *Adv. Mater.* **2010**, *22*, 2694-2697.

[50] Efetov, D. K.; Kim, P. Controlling electron-phonon interactions in graphene at ultrahigh carrier densities. *Phys. Rev. Lett.* **2010**, *105*, 256805.

[51] Lukatskaya, M. R.;Mashtalir, O.;Ren, C. E.;Dall'Agnese, Y.;Rozier, P.;Taberna, P. L.;Naguib, M.;Simon, P.;Barsoum, M. W.; Gogotsi, Y. Cation intercalation and high volumetric capacitance of two-dimensional titanium carbide. *Science* **2013**, *341*, 1502-1505.

[52] Zhan, C.;Naguib, M.;Lukatskaya, M.;Kent, P. R. C.;Gogotsi, Y.; Jiang, D. Understanding the MXene pseudocapacitance. *J. Phys. Chem. Lett.* **2018**, *9*, 1223-1228.

[53] Simon, P.; Gogotsi, Y. Materials for electrochemical capacitors. *Nat. Mater.* **2008**, *7*, 845-854.

[54] Anasori, B.;Xie, Y.;Beidaghi, M.;Lu, J.;Hosler, B. C.;Hultman, L.;Kent, P. R.;Gogotsi, Y.; Barsoum, M. W. Two-dimensional, ordered, double transition metals carbides (MXenes). *ACS Nano* **2015**, *9*, 9507-9516.

[55] Sun, N.;Guan, Z.;Zhu, Q.;Anasori, B.;Gogotsi, Y.; Xu, B. Enhanced ionic accessibility of flexible MXene electrodes produced by natural sedimentation. *Nano-Micro Lett.* **2020**, *12*, 89.

[56] Augustyn, V.;Come, J.;Lowe, M. A.;Kim, J. W.;Taberna, P.-L.;Tolbert, S. H.;Abruña, H. D.;Simon, P.; Dunn, B. High-rate electrochemical energy storage through Li+ intercalation pseudocapacitance. *Nat. Mater.* **2013**, *12*, 518-522.

[57] Wang, G.;Zhang, L.; Zhang, J. A review of electrode materials for electrochemical supercapacitors. *Chem. Soc. Rev.* **2012**, *41*, 797-828.

[58] Wang, B.;Fang, X.;Sun, H.;He, S.;Ren, J.;Zhang, Y.; Peng, H. Fabricating continuous supercapacitor fibers with high performances by integrating all building materials and steps into one process. *Adv. Mater.* **2015**, *27*, 7854-7860.

[59] Guo, Z.;Lu, Z.;Li, Y.; Liu, W. Highly Performed Fiber‐Based Supercapacitor in a Conjugation of Mesoporous MXene. *Adv. Mater. Interfaces* **2022**, *9*, 2101977.

[60] Yu, C.;Gong, Y.;Chen, R.;Zhang, M.;Zhou, J.;An, J.;Lv, F.;Guo, S.; Sun, G. A solid‐state fibriform supercapacitor boosted by host–guest hybridization between the carbon nanotube scaffold and MXene nanosheets. *Small* **2018**, *14*, 1801203.

[61] Yu, D.;Goh, K.;Wang, H.;Wei, L.;Jiang, W.;Zhang, Q.;Dai, L.; Chen, Y. Scalable synthesis of hierarchically structured carbon nanotube–graphene fibres for capacitive energy storage. *Nat. Nanotechnol.* **2014**, *9*, 555-562.

[62] Zhu, Y.;Rajoua, K.;Le Vot, S.;Fontaine, O.;Simon, P.; Favier, F. Modifications of MXene layers for supercapacitors. *Nano Energy* **2020**, *73*, 104734.

[63] Li, L.;Liu, W. D.;Liu, Q.; Chen, Z. G. Multifunctional wearable thermoelectrics for personal thermal management. *Adv. Funct. Mater.* **2022**, *32*, 2200548.

[64] Xu, Y.;Wu, B.;Hou, C.;Li, Y.;Wang, H.; Zhang, Q. Reconfigurable flexible thermoelectric generators based on all‐inorganic MXene/Bi2Te3 composite films. *FlexMat* **2024**, *1*, 248-257.

[65] Wei, M.;Wu, N.;Li, B.;Liu, J.;Pan, F.;Liu, J.; Zeng, Z. From MXene to Multimodal‐Responsive Smart, Durable Electromagnetic Interference Shielding Textiles. *Adv. Funct. Mater.* **2025**, *35*, 2424312.

[66] Liu, L.-X.;Chen, W.;Zhang, H.-B.;Ye, L.;Wang, Z.;Zhang, Y.;Min, P.; Yu, Z.-Z. Super-tough and environmentally stable aramid. Nanofiber@ MXene coaxial fibers with outstanding electromagnetic interference shielding efficiency. *Nano-Micro Lett.* **2022**, *14*, 111.

[67] Shahzad, F.;Alhabeb, M.;Hatter, C. B.;Anasori, B.;Man Hong, S.;Koo, C. M.; Gogotsi, Y. Electromagnetic interference shielding with 2D transition metal carbides (MXenes). *Science* **2016**, *353*, 1137-1140.

[68] Li, M.;Zarei, M.;Mohammadi, K.;Walker, S. B.;LeMieux, M.; Leu, P. W. Silver meshes for record-performance transparent electromagnetic interference shielding. *ACS Appl. Mater. Interfaces* **2023**, *15*, 30591-30599.

[69] Zhou, X.;Min, P.;Liu, Y.;Jin, M.;Yu, Z.; Zhang, H. Insulating electromagnetic-shielding silicone compound enables direct potting electronics. *Science* **2024**, *385*, 1205-1210.

[70] Zhang, D.;Zhang, H.;Cheng, J.;Raza, H.;Liu, T.;Liu, B.;Ba, X.;Zheng, G.;Chen, G.; Cao, M. Customizing coaxial stacking VS 2 nanosheets for dual-band microwave absorption with superior performance in the C-and K u-bands. *J. Mater. Chem. C* **2020**, *8*, 5923-5933.

[71] Iqbal, A.;Sambyal, P.; Koo, C. M. 2D MXenes for electromagnetic shielding: a review. *Adv. Funct. Mater.* **2020**, *30*, 2000883.

[72] Pan, F.;Shi, Y.;Yang, Y.;Guo, H.;Li, L.;Jiang, H.;Wang, X.;Zeng, Z.; Lu, W. Porifera‐inspired lightweight, thin, wrinkle‐resistance, and multifunctional MXene foam. *Adv. Mater.* **2024**, *36*, 2311135.

[73] Liu, J.;Luo, H.;Wang, G.;Han, S.;Li, K.;Zhang, Y.;Liu, X.;Ye, F.; Xu, Y. In-situ derive hierarchical Ti3C2@C@ZnO heterointerface for electromagnetic absorption enhancement. *Nano Res.* **2025**, *18*, 94907168.

Electronic Supplementary Material

Fe^{2+}-crosslinked MXene fibers for multifunctional electronic textile

Wenkun Fei [1,2,§], Xuejiao Wang[2,§], Chaoyang Miao[2,§], Jiahao Chen[2], Shujuan Liu[1], Bingxiang Li [2] ✉, Jianmin Li [1,2] ✉, and Qiang Zhao [1,2] ✉

[1] *State Key Laboratory of Flexible Electronics (LoFE) & Institute of Advanced Materials (IAM), Nanjing University of Posts & Telecommunications, Nanjing 210023, China*
[2] *College of Electronic and Optical Engineering & College of Flexible Electronics (Future Technology), Nanjing University of Posts & Telecommunications, Nanjing 210023, China*
[§] *Wenkun Fei, Xuejiao Wang, and Chaoyang Miao contributed equally to this work.*

Supporting information to https://doi.org/10.26599/NR.2026.94908426

Address correspondence to Bingxiang Li, bxli@njupt.edu.cn; Jianmin Li, lijm@njupt.edu.cn; Qiang Zhao, iamqzhao@njupt.edu.cn

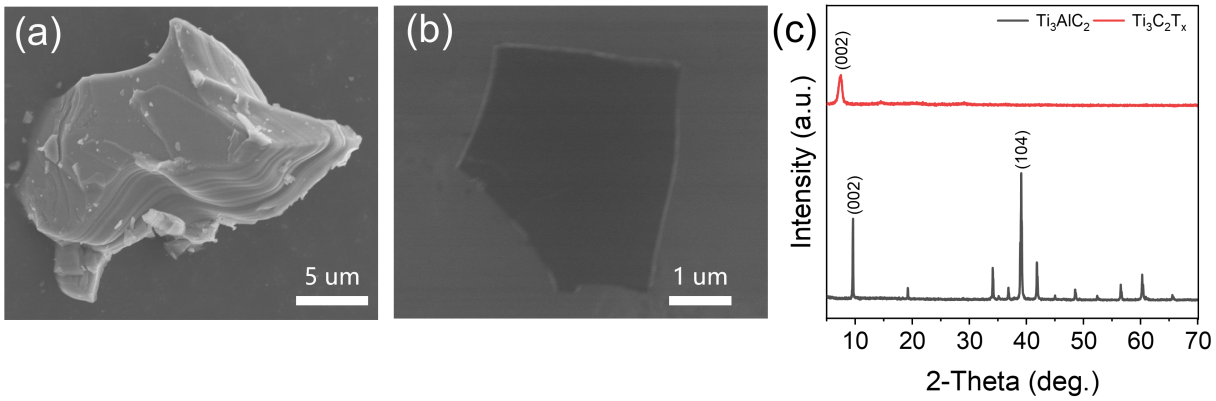

Figure S1. The synthesis of $Ti_3C_2T_x$ nanosheets. The SEM images of (a) commercial Ti_3AlC_2 MAX bulk and (b) the as-synthesized $Ti_3C_2T_x$ nanosheet. (c) XRD patterns of Ti_3AlC_2 bulks and $Ti_3C_2T_x$ film.

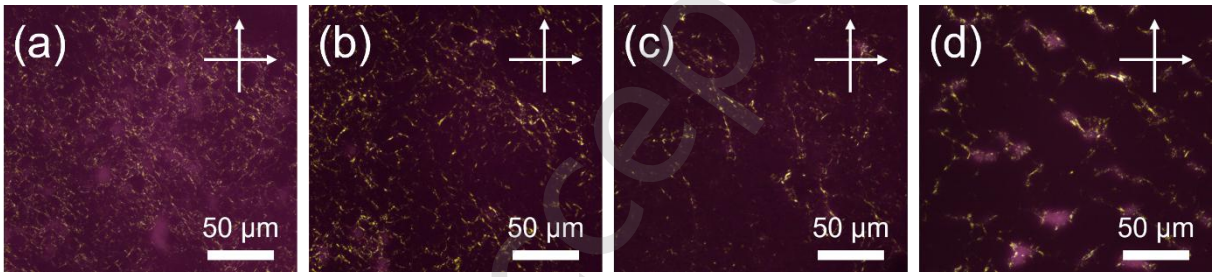

Figure S2. POM images of MXene dispersion of (a) 40 mg mL^{-1}, (b) 60 mg mL^{-1}, (c) 100 mg mL^{-1}, (d) 120 mg mL^{-1}.

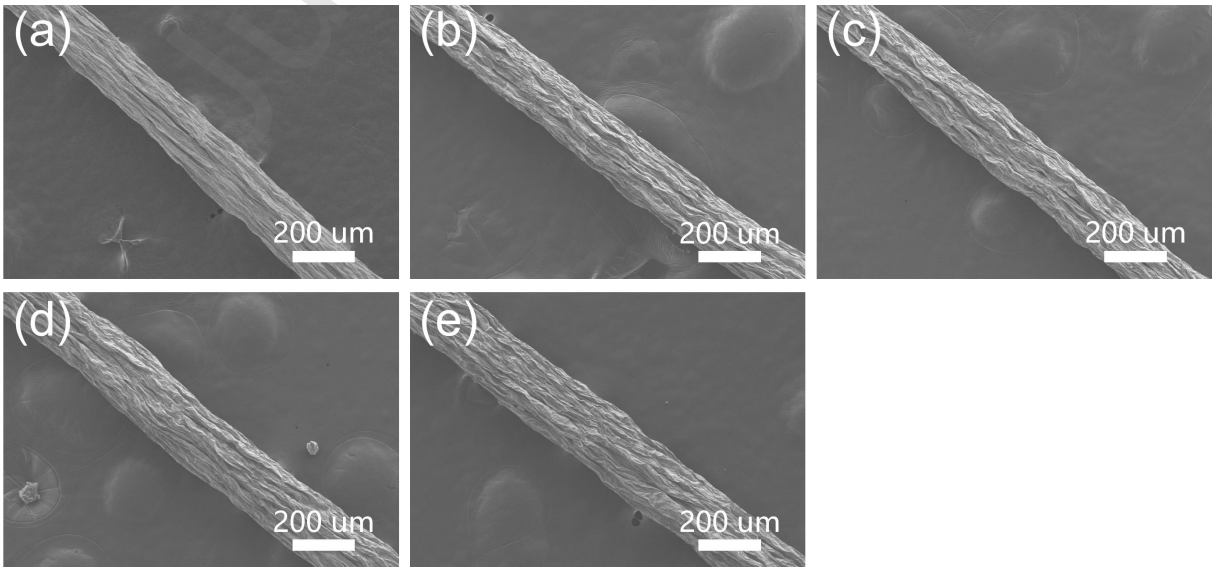

Figure S3. SEM images of (a) MF-0.1, (b) MF-0.2, (c) MF-0.3, (d) MF-0.4, (e) MF-0.5.

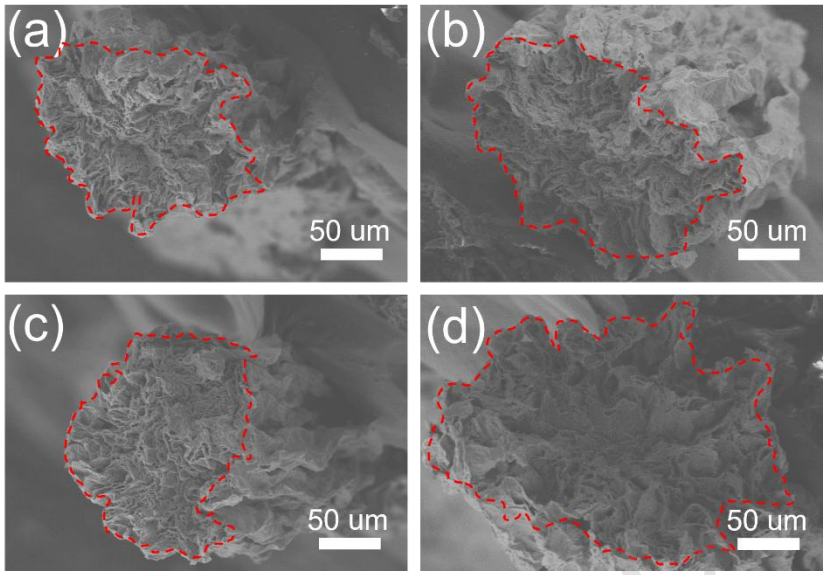

Figure S4. Cross-sectional SEM images of (a) MF-0.2, (b) MF-0.3, (c) MF-0.4, (d) MF-0.5.

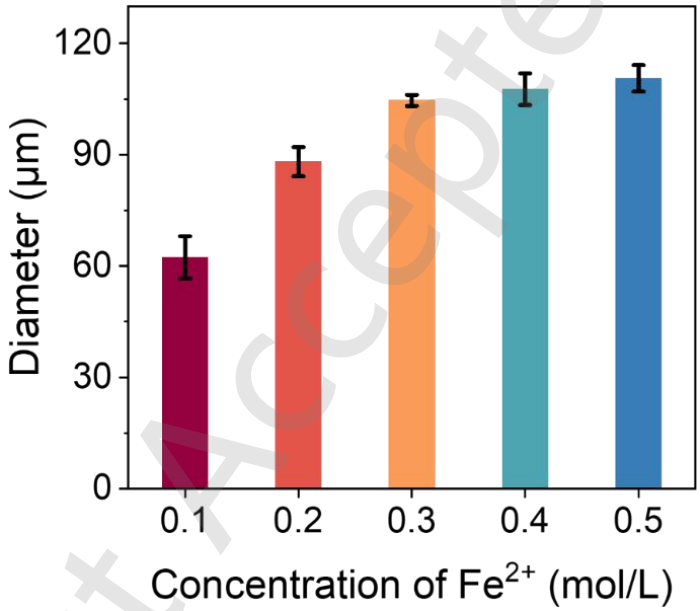

Figure S5. The statistical diameters of MF fibers prepared in different $FeCl_2$ concentrations.

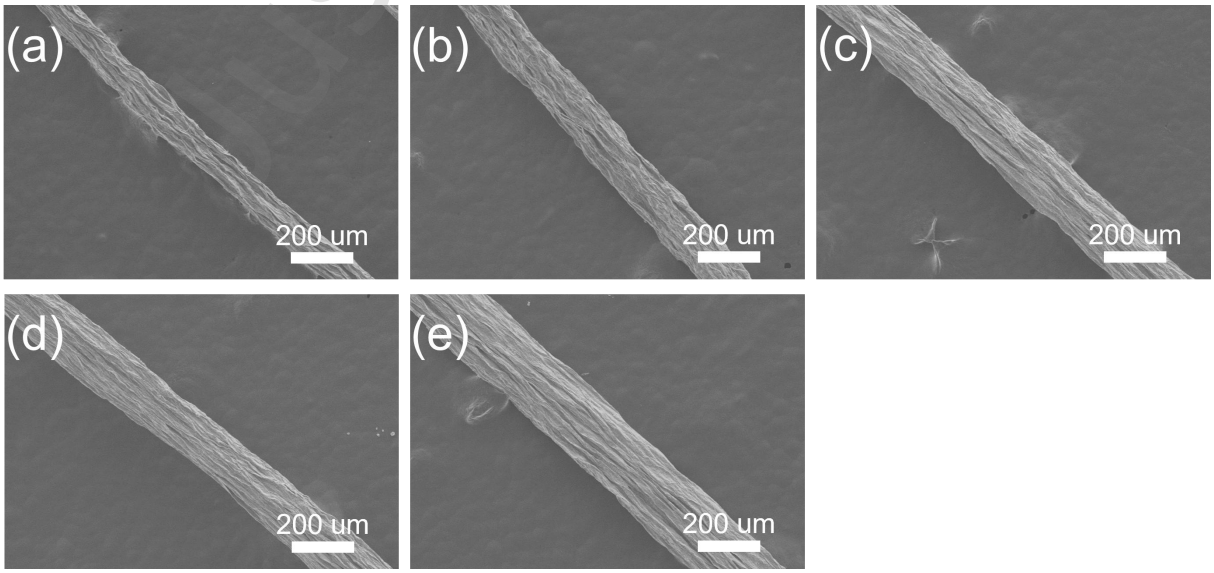

Figure S6. SEM images of MXene fibers prepared from spinning dope with different MXene ink concentrations: (a) 40 mg mL^{-1}; (b) 60 mg mL^{-1}; (c) 80 mg mL^{-1}; (d) 100 mg mL^{-1}; (e) 120 mg mL^{-1}.

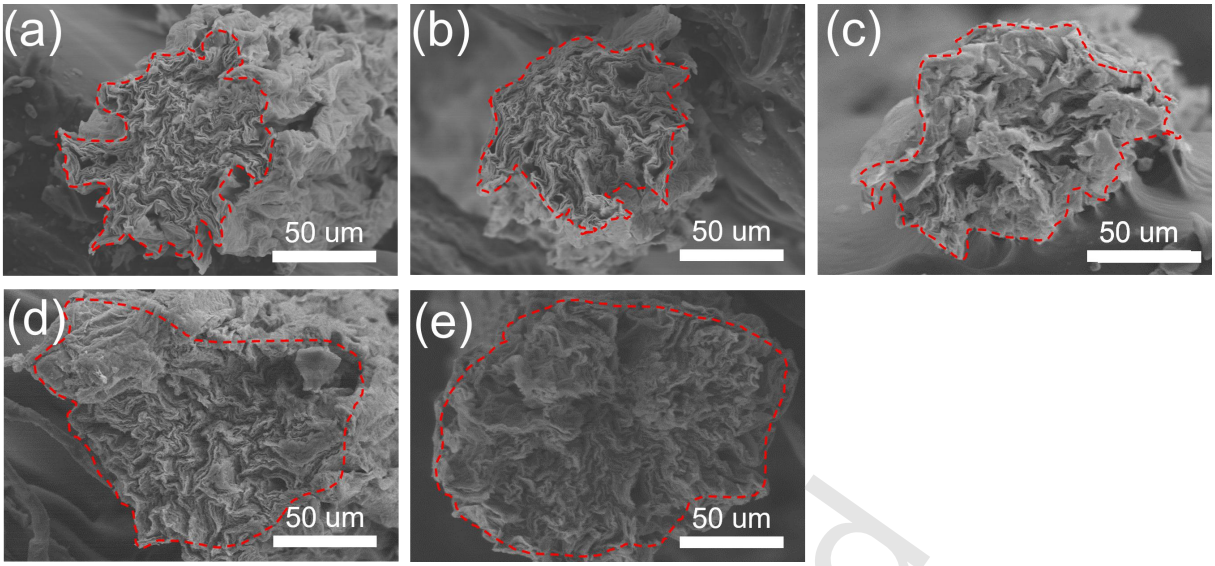

Figure S7. Cross-sectional SEM images of MXene fibers prepared from spinning dope with different MXene ink concentrations: (a) 40 mg mL^{-1}; (b) 60 mg mL^{-1}; (c) 80 mg mL^{-1}; (d) 100 mg mL^{-1}; (e) 120 mg m

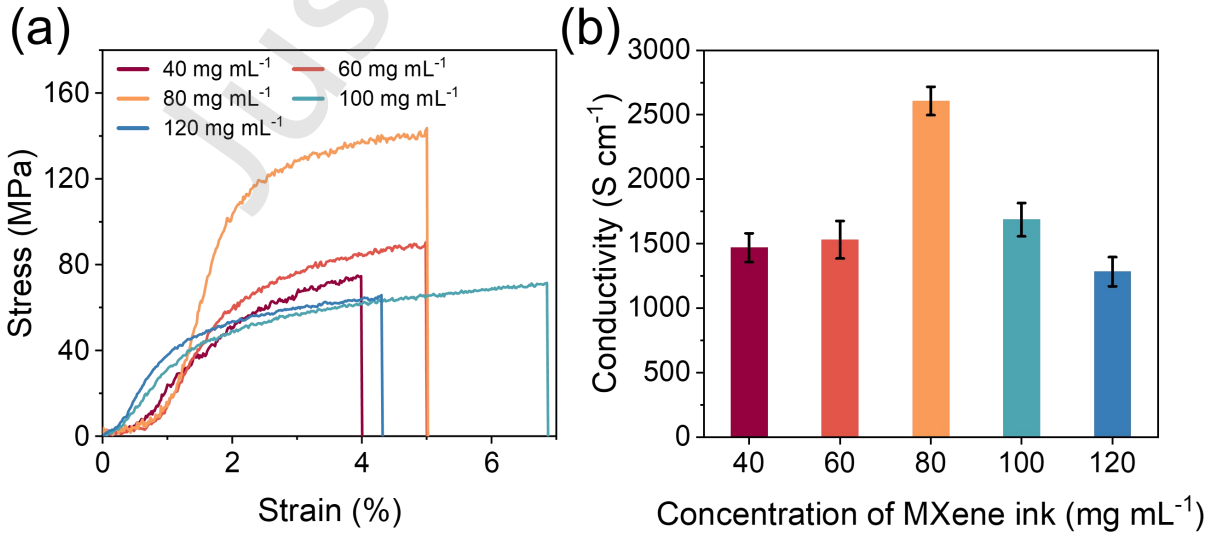

Figure S8. (a) Stress-strain curves and (b) electrical conductivity of $Ti_3C_2T_x$ MXene fibers prepared from spinning dopes with different MXene ink concentrations.

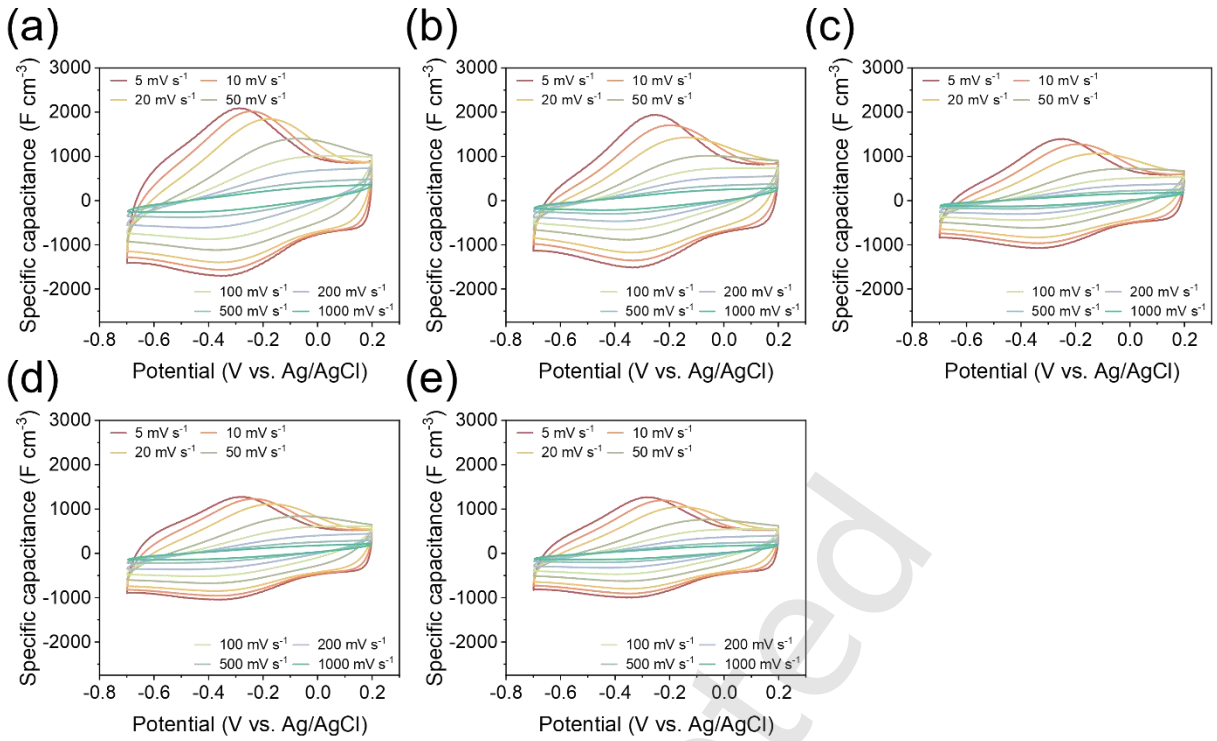

Figure S9. The CV curves of (a) MF-0.1, (b) MF-0.2, (c) MF-0.3, (d) MF-0.4, (e) MF-0.5 at various scan rates.

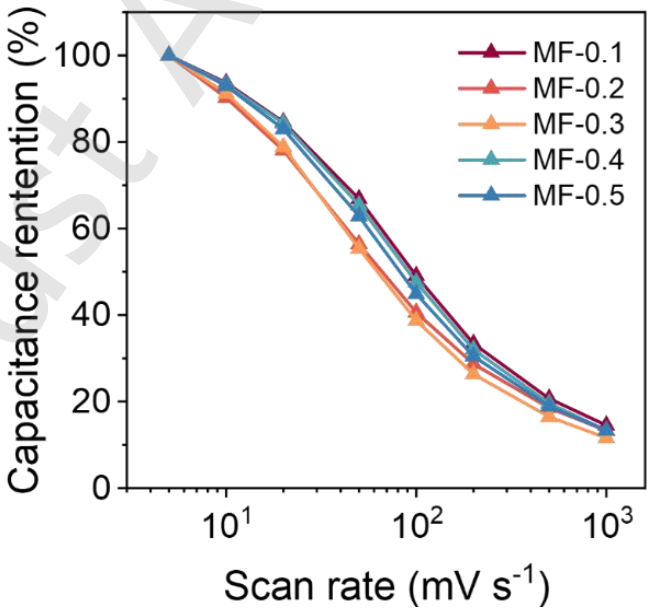

Figure S10. Specific capacitance values of MF fibers at different scan rates.

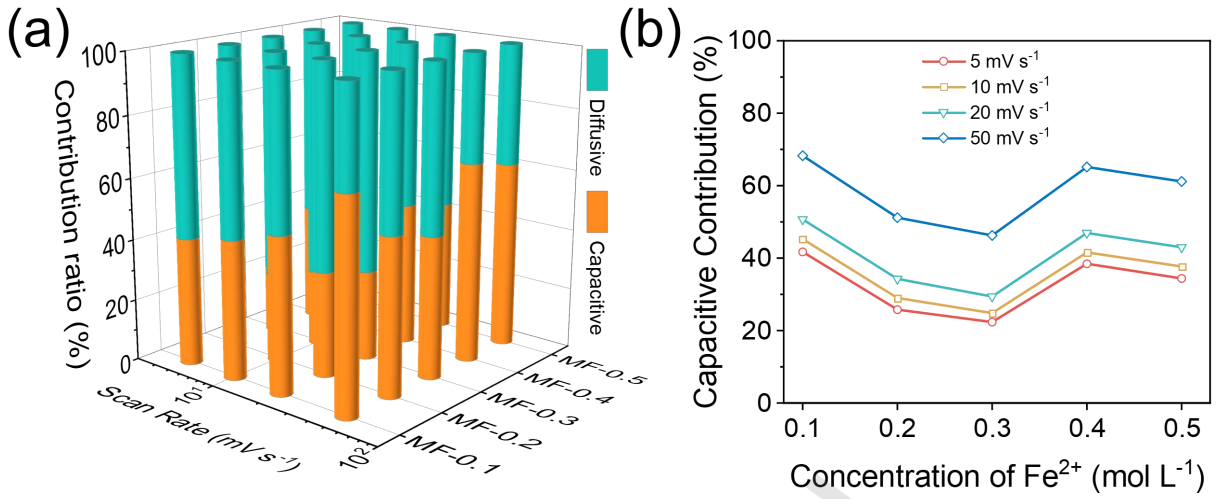

Figure S11. (a) Contribution ratio of capacitive-controlled and diffusion-controlled capacitance of MF-X fibers at various scan rates. (b) Capacitive contribution of MF-X fibers at various scan rates.

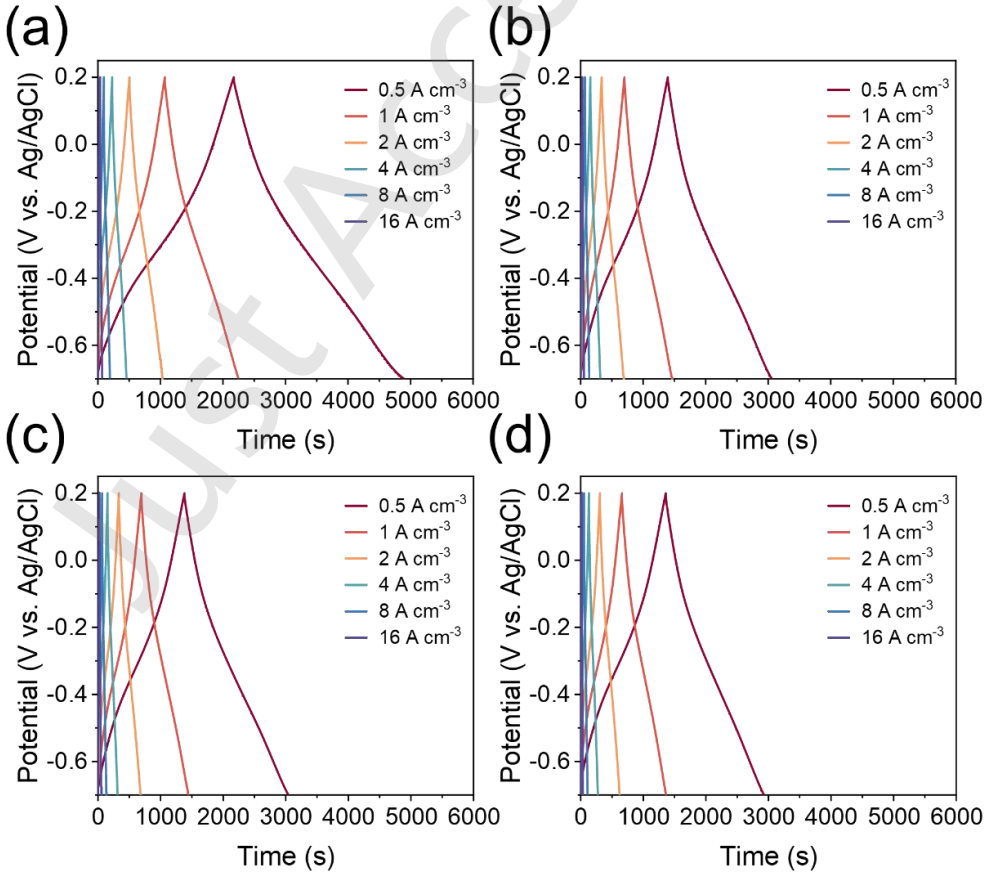

Figure S12. The GCD curves of (a) MF-0.2, (b) MF-0.3, (c) MF-0.4, (d) MF-0.5 at various scan rates.

Figure S13. The digital image of an assembled MF-based supercapacitor.

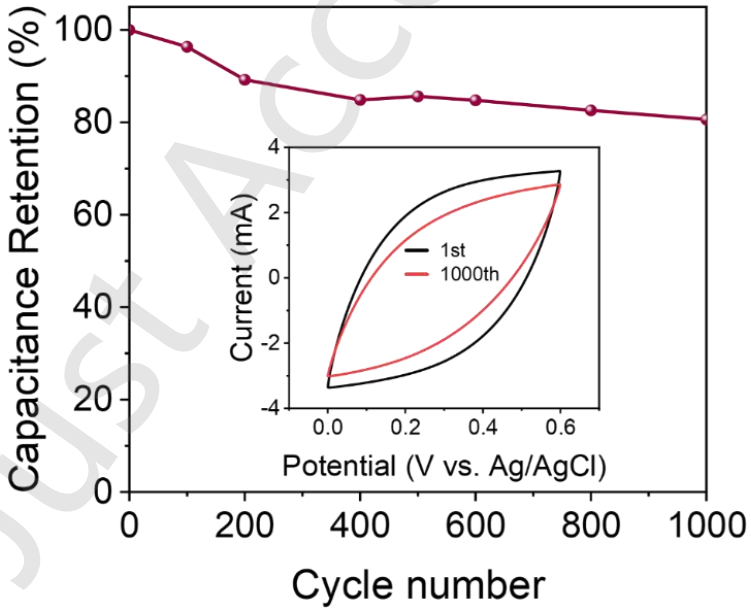

Figure S14. Cyclic stability of the MF-based supercapacitor over 1000 cycles, with the inset showing the CV curves for the 1st and 1000th cycle.

Table S1. Comparison of the Physical and Mechanical Property Parameters of MF-X Fibers.

Samples	Diameter (μm)	Density (g cm^{-3})	Tensile Strength (MPa)	Tensile Elongation (%)	Young's Modulus (GPa)	Tensile Toughness (MJ m^{-3})
MF-0.1	62.32	2.62	143.7	5.00	10.4	4.57
MF-0.2	88.13	2.24	75.8	4.22	4.1	1.81
MF-0.3	104.64	2.24	56.3	3.30	3.6	0.91
MF-0.4	107.64	2.20	54.7	2.75	3.5	0.75
MF-0.5	110.56	1.92	51.9	2.73	2.8	0.73

Table S2. Comparison of the Electrothermal Performance of MXene-Based Fibers.

Fibers	Voltage (V)	Initial Temperature (°C)	Saturation Temperature (°C)	ΔT/V (°C V^{-1})	Response Time (Δt)	ΔT/Δt (°C min^{-1})	Response Time (to 60°C)	Ref
MXene@ANF fiber	21	25	123	4.67	10 s	588.2	1.6 s	S1
Zn^{2+}-crosslinked $Ti_3C_2T_x$ fiber	10	32	144.1	11.21	3 s	2242	<0.5 s	S2
Mg^{2+}-crosslinked $Ti_3C_2T_x$ fiber	12	15	103	7.33	<1 s	46800	<0.5 s	S3
Additive-free MXene fiber	24	26	68	1.75	0.07 s	36000	<0.5 s	S4
Fe^{2+}-crosslinked $Ti_3C_2T_x$ fiber	2	25	122	48.5	2 min	48.5	28 s	**This work**

Table Footnotes*:*

[a] ANF represents sodium aramid nanofibers.

[b] ΔT/V refers to the ratio of the maximum temperature difference during the electrothermal process to the applied voltage; Response Time refers to the time required to reach the saturation temperature from the initial temperature; Response Time (to 60°C) refers to the time required to reach 60°C from the initial temperature.

Table S3. Comprehensive comparison of MXene fiber-based EMI shielding fabrics

Fibers	Conductivity (S cm^{-1})	Grid size (mm)	Thickness (mm)	EMI SE (dB)	Ref
Fe^{2+}-crosslinked $Ti_3C_2T_x$ fiber	2607	1×1	~0.32	23.1	**This work**
ANF@MXene fiber	3000	1×1	0.071	31.5	[S5]
RC@MXene fiber	368	1×1	0.004	~30	[S6]
CNT@MXene fiber fabrics	0.4	plain weave fabrics	1.19	23.4	[S7]
Non-woven MXene fiber fabrics	708	Like film	0.107	75.0	[S8]
MXene@CF composite	163	layered CF fabric	2	34.4	[S9]

Table Footnotes:

CNT represents carbon nanotube; CF represents carbon fiber; RC represents regenerated cellulose; ANF represents aramid nanofiber.

Reference

[S1] Liu, Y.; Kumar, S. Polymer/carbon nanotube nano composite fibers–a review. *ACS Appl. Mater. Interfaces* **2014**, *6*, 6069-6087.

[S2] Cao, X.;Wu, G.;Li, K.;Hou, C.;Li, Y.;Zhang, Q.; Wang, H. High‐Performance Zn2+‐Crosslinked MXene Fibers for Versatile Flexible Electronics. *Adv. Funct. Mater.* **2024**, *34*, 2407975.

[S3] Li, S.;Fan, Z.;Wu, G.;Shao, Y.;Xia, Z.;Wei, C.;Shen, F.;Tong, X.;Yu, J.; Chen, K. Assembly of nanofluidic MXene fibers with enhanced ionic transport and capacitive charge storage by flake orientation. *ACS Nano* **2021**, *15*, 7821-7832.

[S4] Zhang, J.;Uzun, S.;Seyedin, S.;Lynch, P. A.;Akuzum, B.;Wang, Z.;Qin, S.;Alhabeb, M.;Shuck, C. E.; Lei, W. Additive-free MXene liquid crystals and fibers. *ACS Cent. Sci.* **2020**, *6*, 254-265.

[S5] Liu, L.;Chen, W.;Zhang, H.;Ye, L.;Wang, Z.;Zhang, Y.;Min, P.; Yu, Z. Super-Tough and Environmentally Stable Aramid. Nanofiber@MXene Coaxial Fibers with Outstanding Electromagnetic Interference Shielding Efficiency. *Nano-Micro Lett.* **2022**, *14*, 111.

[S6] Liu, L.;Chen, W.;Zhang, H.;Zhang, Y.;Tang, P.;Li, D.;Deng, Z.;Ye, L.; Yu, Z. Tough and electrically conductive Ti3C2Tx MXene-based core-shell fibers for high-performance electromagnetic interference shielding and heating application. *Chem. Eng. J.* **2022**, *430*.

[S7] Feng, W.;Zou, L.;Lan, C.;E, S.; Pu, X. Core-Sheath CNT@MXene Fibers Toward Absorption-Dominated Electromagnetic Interference Shielding Fabrics. *Adv. Fiber Mater.* **2024**, *6*, 1657-1668.

[S8] Xiong, J.;Zheng, H.;Ding, R.;Li, P.;Liu, Z.;Zhao, X.;Xue, F.;Chen, Z.;Yan, Q.;Peng, Q.; He, X. Multifunctional non-woven fabrics based on interfused MXene fibers. *Mater. Des.* **2022**, *223*.

[S9] Hu, Y.;Chen, J.;Yang, G.;Li, Y.;Dong, M.;Zhang, H.;Bilotti, E.;Jiang, J.; Papageorgiou, D. G. Highly conductive and mechanically robust MXene@ CF core-shell composites for in-situ damage sensing and electromagnetic interference shielding. *Compos. Sci. Technol.* **2024**, *246*, 110356.